2004

Probing the Interstellar Medium on AU Size Scales Using Pulsar Scintillation

Alexander S. Hill
Oberlin College

Probing the Interstellar Medium on AU Size Scales Using Pulsar Scintillation

Alex S. Hill

April 23, 2004

An Honors thesis presented to the Department
of Physics and Astronomy of Oberlin College

Contents

List of Figures

List of Tables

Acknowledgements

Like all scientific work, this was a collaborative process. Wendy Everett and Natalie Hinkel were my observing companions in the wee hours of the morning and are responsible for much of the data processing and analysis. Curtis Asplund, Dan Berwick, and Max Rudolph have provided valuable assistance in developing and completing this project.

Dan Stinebring has served as my advisor, mentor, teacher, and friend for three years. I thank him for dedicating himself to helping all his students become better scientists and people. I would not be where I am today without him.

This project relies heavily on data from the Arecibo Observatory, a part of the National Astronomy and Ionosphere Center,[1] which is operated by Cornell University under a cooperative agreement with the National Science Foundation. I thank the telescope operators and support staff at Arecibo for their assistance in making sure our observations went as smoothly as possible and for continuing to improve this extraordinary instrument.

[1] `http://www.naic.edu`

Chapter 1

Introduction

1.1 The Interstellar Medium

The *Interstellar Medium* (ISM) is the 'stuff' in the space between stars. The ISM is dominated by diffuse gases, mostly atomic hydrogen; it also has significant amounts of molecular hydrogen and ionized hydrogen. The ionized component of the ISM (IISM) has a mean electron density $n_0 \sim 0.005$ cm^{-3} (McKee & Ostriker, 1977).

The ISM is turbulent. The turbulence ranges in size scale from the large-scale structures that input energy into the medium (the *outer scale*) to the size at which turbulence dissipates as heat (the *inner scale*). This turbulence cascade may extend over a range of up to 12 orders of magnitude in size. The range of turbulent size scales creates structure in the ISM, but the size and and dissipation time scales of these structures are not well understood.

The primary observable effect of free electrons in the ISM is scattering of passing radio waves. Therefore, to probe the medium, we need a source of radiation to illuminate it. These observations are simpler and provide more detailed information if the radio source is coherent, which leads to interference effects. In addition, a substantial transverse velocity is useful because the line of sight to the source moves through the medium, allowing measurements of the spatial variation of scattering features. Pulsars meet these criteria well.

1.2 Pulsars

First discovered in 1967 by Jocelyn Bell and Anthony Hewish, pulsars are neutron stars that rotate rapidly, with periods $\lesssim 2$ s. A narrow cone of electromagnetic radiation (typically at radio wavelengths) is emitted from two poles of the neutron star. Because of the rotation of the pulsar, these cones of radiation appear to a distant observer as 'pulses' of radio power, analogous to a lighthouse.

Neutron stars are collapsed stars with masses $\gtrsim 1.4\,M_\odot$[1]. As the progenitor star collapses, a large amount of energy is released. The release of energy is rarely perfectly symmetric, so the newly formed pulsar is given a large kick, resulting in velocities of hundreds of kilometers per second. Pulsars have radii of order 10 km and densities of $\sim 10^{14}$ g cm^{-3}.

The radius of the light cylinder, r_{lc} is the distance at which a particle with the angular velocity of the pulsar is traveling at the speed of light:

$$r_{lc} = \frac{cP}{2\pi},$$

where P is the period of the pulsar. For a typical pulsar, $P \approx 1$ s, implying $r_{lc} \approx 5 \times 10^4$ km. At radial distances $\lesssim r_{lc}$ there is a co-rotating magnetosphere of high energy plasma; the emission is from within this region (Lyne & Graham-Smith, 1990). Therefore, at a distance of > 100 pc for the nearest known pulsars, pulsars have an angular size of $< 10^{-14}$ radians, or 1 nas. For radio astronomical observations, these are point sources.

Pulsars have extraordinarily regular periods, usually known observationally to one part in 10^{15}. Rotational energy loss causes measurable spindown; the corresponding increase in pulsar periods is also consistent and well-measured. Typical period time derivatives are $\dot{P} \sim 10^{-14}$ (in dimensionless units), or 10^{-7} s yr^{-1}.

For our purposes, pulsars are bright radio sources of coherent radiation that serve as excellent probes of the IISM. The turbulent IISM causes multi-path propagation of the radio waves emitted by pulsars. Because pulsars are point sources, the waves are initially coherent. The combination of these factors gives rise to interference, which is observable as a frequency dependent fluctuation in the intensity of the source as observed by a terrestrial radio telescope. Because of the high transverse velocity of pulsars, the interference pattern changes in time as the pulsar moves through the medium. These interference effects also give rise to modulations in the source intensity, or *scintillation*. For the remainder of this work, we use the term "scintillation" to refer to all interference-related effects.

1.2.1 Pulsar distance and proper motion measurements

Throughout astrophysics, distances are notoriously difficult to measure. The only direct distance measurement technique is parallax: the angular shift of the source, relative to a background source, due to the Earth's orbital motion about the sun. This method only works for sources near enough to the Earth to have a measurable angular shift; at radio frequencies and typical pulsar distances, parallax measurements can be made using very long baseline interferometry (VLBI) techniques out

[1] One solar mass, $1\,M_\odot = 2.0 \times 10^{33}$ g, is the conventional unit of mass in astrophysics. For relatively small masses and distances, *cgs* units are commonly used. Angles are typically expressed in arcseconds (as). The conventional units of length are the astronomical unit (AU) and the parsec (pc). One AU is the mean distance from the Earth to the Sun, or 1.49×10^{13} cm. One parsec is the distance to an object 1 AU in size with a parallax angle of 1 as, or 3.1×10^{18} cm $= 3.3$ light years. Stellar parallax is the change in angular position of a source due to the orbital movement of the Earth. Velocities are typically expressed in km s^{-1}.

to a maximum distance of $D \sim 1$ kpc. Significant improvements in observational techniques for measuring parallax have been made in the last five years, led by Brisken et al. (2002).

When no parallax measurements are available, the best method of determining pulsar distances is to use a measurement of the electron content along the line of sight to the pulsar. This method is discussed in section 2.1.

Pulsar proper motion velocities, μ can be directly measured, in units of angle per time, to good accuracy. Proper motion is converted to velocity (in units of km s^{-1}) by $V_{\mathrm{p},\perp} = \mu D$, so velocity estimates are subject to the same uncertainties as distance measurements.

1.3 Observations

We observe pulsars primarily using the Arecibo Observatory, a 305 m diameter radio telescope near Arecibo, Puerto Rico. Through a combination of archival data going back to 1980 and previous observing campaigns undertaken by our group from 1999-2003 (Stinebring et al., 2001; Hill et al., 2003), we have over 1000 high quality scintillation observations of 20 pulsars. In this work, our primary data source is a new data set obtained at Arecibo during 2004 January.

1.3.1 Observing technique and data processing

The telescope "backend" spectrometer records radio *flux density*, or power per unit frequency per unit collecting area. The conventional unit of flux density is the Jansky: 1 Jy $= 10^{-26}$ W m^{-2} Hz^{-1}. We principally use three receivers: the 327 MHz receiver, with a frequency range of 312–342 MHz, the 430 MHz receiver, with a frequency range of 423–438 MHz, and the L-band wide receiver, with a frequency range of 1.15–1.73 GHz.[2] We use the Wideband Arecibo Pulsar Processor (WAPP)[3] spectrometer. There are four WAPP spectrometers which collect data simultaneously, allowing observers to collect data in four bands within the receiver band. Each WAPP has 1024 frequency channels.[4] In our observations, the spectrometer sums data for 4096 μs and then outputs to disk.

In post-processing, we divide the observation into time intervals of the length of the pulsar period. Each pulsar period is divided into 128 'phase bins,' and successive periods are summed into 10 second 'chunks' to improve the signal to noise ratio. In this step, we also *dedisperse* the data to correct for the frequency-dependent time delay of radio waves due to the IISM (see Section 2.1). The observation is now reduced to a data cube containing ~ 360 planes (for a 3600 s observation), each 128 phase bins $\times$ 1024 channels, representing 10 s of data as a function of observing frequency and pulsar phase. One such plane is shown in Figure 1.1.

With this data cube, we select the phase bins that correspond to the 'on-pulse' power and sum that power for each frequency channel. The power in an off pulse spectrum is subtracted from the

[2]See `http://www.naic.edu/~astro/RXstatus/rcvrtabz.shtml`

[3]See `http://www.naic.edu/~wapp`

[4]The WAPPs were upgraded to accomodate 2048 frequency channels in late January 2004.

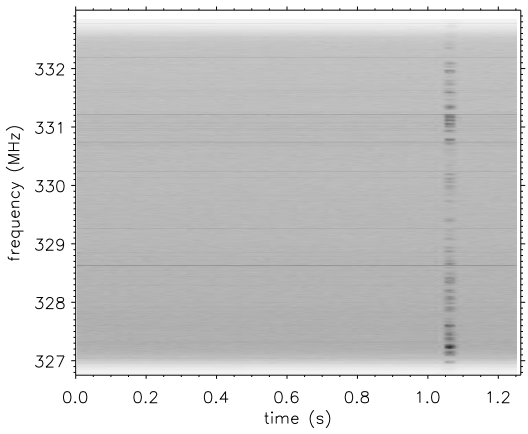

Figure 1.1: One 10 s chunk of dedispersed data, summed modulo the pulsar period. The horizontal axis corresponds to pulsar phase. The intensity of the pulsar is represented by the grayscale. The variations in pulse intensity with frequency are the effects of scintillation, the primary focus of this work. Horizontal stripes at a fixed frequency are radio frequency interference.

on-pulse spectrum to remove the background and most radio frequency interference (both of which have periods independent of the pulsar period). This difference is divided by the off pulse spectrum to flatten the baseline and correct for variations in the sensitivity of the receiver across the band.

1.3.2 Dynamic spectrum

We now have a *dynamic spectrum*, $S(\nu, t)$, which consists of spectra, each representing 10 seconds of on-pulse data, laid out side by side up to the length of the observation. A typical dynamic spectrum is shown in Figure 1.2

The modulations in intensity over frequency within each spectrum are due to *scintillation*, interference between phase delayed rays. The changes to the interference pattern over time are due to the movement of the pulsar past different portions of the scattering medium. Although these variations are evident in the dynamic spectrum, they are more convenient to analyze and interpret in the transform domain.

1.3.3 Secondary spectrum

The two dimensional Fourier transform of the dynamic spectrum multiplied by its complex conjugate, $P(f_\nu, f_t) = |\tilde{S}(\nu, t)|^2$, is called the power spectrum, or *secondary spectrum*, of the dynamic (Rickett et al., 1997). The transform variables are conjugate frequency, f_ν, and conjugate time, f_t. An example secondary spectrum is shown in Figure 1.3. Intensity in the secondary spectrum is plotted

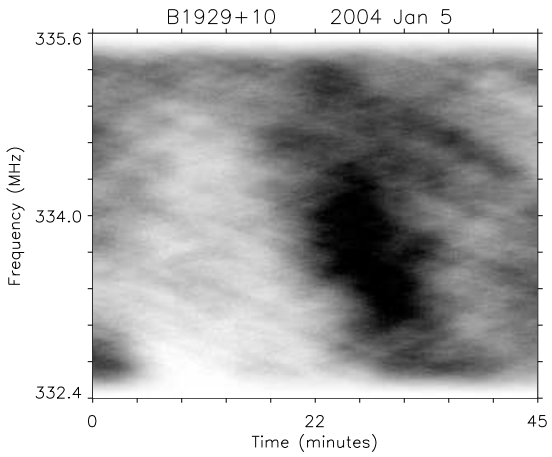

Figure 1.2: A typical dynamic spectrum of PSR B1929 + 10. The grayscale is linear in intensity, with dark representing the strongest intensity.

as a logarithmic grayscale to accentuate faint features; black corresponds to 5 dB below the most intense point, and white corresponds to 3 dB above peak of the noise. Because the input (dynamic) spectrum is real, the secondary spectrum is symmetric under reflection about the origin, so we do not normally plot the redundant lower half-plane ($f_\nu < 0$).

The secondary spectrum identifies periodicities in the dynamic spectrum. Large periodicities (with small frequencies) in the dynamic are represented by points near the origin of the secondary, while fine periodicities appear far from the origin of the secondary. This means that small features in the dynamic appear far from the origin in the secondary, and vice versa.

1.4 Thin Screen Model

Our model has been developed over the past four years by Stinebring et al. (2001); Becker (2001); Kramer (2001); Reeves (2003); Hill et al. (2003); Walker et al. (2004); and Cordes et al. (2004). Data presented in these papers and earlier studies lead us to assume that the scattering is dominated by a 'thin screen' perpendicular to the line of sight to the pulsar. A 'thin' screen means that the screen is thin compared to the distance of the pulsar; this condition is satisfied by a fractional thickness of ~ 0.01–0.05. For a typical pulsar distance of 300 pc, this implies a screen thickness of $\sim$ 3–15 pc. Although it seems somewhat implausible that thin screens of material are distributed throughout interstellar space, there are several natural models that explain these structures. For example, supernova shock waves and sharp boundaries between ionized and unionized regions of the ISM each lead to a confined region of turbulent plasma.

The geometry of scattering is sketched in Figure 1.4. The pulsar is a distance D from the

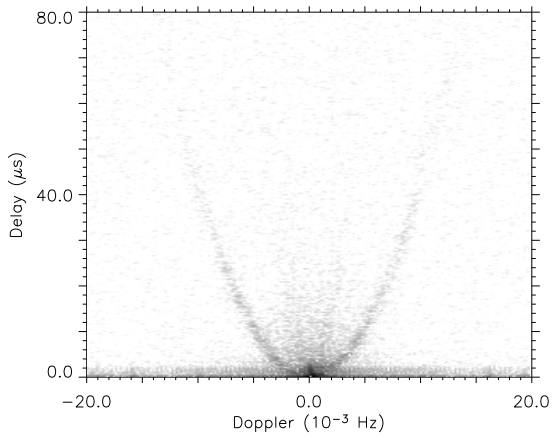

Figure 1.3: The secondary spectrum of Figure 1.2. Note the sharply delineated parabolic arc, which represents periodicities in the dynamic spectrum. The parabolic feature was first identified by the Oberlin group in 1999 (Stinebring et al., 2001).

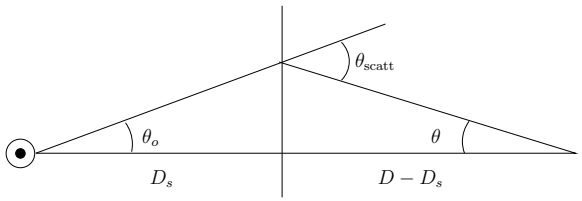

Figure 1.4: The geometry of scattering in our model.

observer. A ray emerging from the pulsar at an angle θ_0 intersects the screen (a distance D_s from the pulsar) and is scattered by some mechanism through an angle $\theta_{\rm scatt}$ towards the telescope. The observed angle is $\theta = \theta_{\rm scatt} - \theta_0$.

1.4.1 Pulsar image

A pulsar cannot be imaged directly. Instead, we are left to infer the appearance of the image by examining scintillation data. In our model, the image typically consists of a bright, scatter-broadened core at the geometrical location of the pulsar and a broad halo of scattered rays. This image profile naturally arises from a Kolmogorov turbulence spectrum (Walker et al., 2004; Cordes et al., 2004). At small scattering angles, a Kolmogorov angular spectrum is similar to a Gaussian; we schematically refer to this region as the 'core' of the image. At large scattering angles, a Kolmogorov spectrum has broad 'wings' of faint power (whereas a Gaussian falls off quickly to essentially zero scattering power); this is the region we refer to as the 'halo' of the image. The interference pattern

seen in dynamic and secondary spectra is due to interference between the core and the halo; the self-interference term of the core with itself is represented by a confined region of very high intensity at the origin of the secondary spectrum, while interference between any two points in the halo is too weak to detect.

We define an image coordinate system with the origin located at the geometrical position of the pulsar and the $\hat{\boldsymbol{x}}$ axis lying along the pulsar velocity vector. The $\hat{\boldsymbol{y}}$ axis is perpendicular to the $\hat{\boldsymbol{x}}$ axis in the image plane, and the $\hat{\boldsymbol{z}}$ axis points from the pulsar to the observer. An arbitrary coordinate in the image is given by $\boldsymbol{\theta} = \theta_x \hat{\boldsymbol{x}} + \theta_y \hat{\boldsymbol{y}}$.

1.4.2 Differential time delay

The geometric path length difference between two scattered paths with observed angles $\boldsymbol{\theta}_1$ and $\boldsymbol{\theta}_2$ is (Appendix A)[5]

$$\Delta\mathcal{L} = \frac{D(\theta_2^2 - \theta_1^2)}{2}\left(\frac{1-\beta}{\beta}\right),$$

where $\beta \equiv D_s/D$ is the fractional distance of the screen from the pulsar ($\beta = 0$) to the observer ($\beta = 1$). The difference in arrival time between the two rays is $\Delta\tau = \Delta\mathcal{L}/c$. This *differential time delay* corresponds to the conjugate frequency axis of the secondary spectrum (Walker et al., 2004). Therefore, the conjugate frequency due to interference between two points in the image plane is

$$f_\nu = \Delta\tau = \frac{D}{2c}\left(\frac{1-\beta}{\beta}\right)\left(\theta_2^2 - \theta_1^2\right). \tag{1.1}$$

Because of this equality, we hereafter refer interchangeably to the conjugate frequency and the delay axis of the secondary spectrum.

1.4.3 Differential Doppler shift

Scattered rays are Doppler shifted as they pass through the screen. The frequency at the scattering screen, ν_s, is related to the frequency emitted by the pulsar, ν_e, by (Reeves, 2003, Chapter 2)

$$\nu_s = \left(\frac{1 + \boldsymbol{V}_{\mathrm{eff},\perp} \cdot \boldsymbol{\theta}_p}{c}\right)\nu_e, \tag{1.2}$$

where

$$\boldsymbol{V}_{\mathrm{eff},\perp} \equiv (1-\beta)\boldsymbol{V}_{\mathrm{p},\perp} + \beta\boldsymbol{V}_{\mathrm{obs},\perp} - \boldsymbol{V}_{\mathrm{screen},\perp} \tag{1.3}$$

[5]Throughout this work, we are considering angles that are, at most, on the order of milliarcseconds, so small angle approximations hold.

is the effective velocity of the pulsar (Cordes & Rickett, 1998).[6] The same Doppler shift then applies between the screen and the observer:

$$\nu_{\rm obs} = \left(\frac{1 + \boldsymbol{V}_{\rm eff,\perp} \cdot \boldsymbol{\theta}}{c}\right) \nu_e,$$

where $\nu_{\rm obs}$ is the observed frequency. The differential transverse Doppler shift between two points $\boldsymbol{\theta}_1$ and $\boldsymbol{\theta}_2$ in the image is thus given by

$$f_t = \frac{1}{\lambda\beta}(\boldsymbol{\theta}_2 - \boldsymbol{\theta}_1) \cdot \boldsymbol{V}_{\rm eff,\perp}, \tag{1.4}$$

which corresponds to the conjugate time in the secondary spectrum.

1.4.4 Scintillation arcs

In this model, the intensity at each coordinate (f_t, f_ν) in the secondary spectrum corresponds to the product of the intensities of pairs of points $\boldsymbol{\theta}_1$ and $\boldsymbol{\theta}_2$.[7] We make the reasonable assumption that the image is dominated by a bright core near the origin (the geometrical position of the pulsar), so interference between the relatively weak points not at the origin is negligible. Therefore, we fix $\boldsymbol{\theta}_1 = \boldsymbol{0}$. We also make the assumption that the velocity of the pulsar (typically $V_{\rm p,\perp} \sim 300$ km s^{-1}) is much greater than the orbital velocity of the Earth ($V_{\rm obs,\perp} \approx 30$ km s^{-1}) or the screen (typically $V_{\rm screen,\perp} \sim 10$ km s^{-1}). Thus, $\boldsymbol{V}_{\rm eff,\perp} \approx (1-\beta)\boldsymbol{V}_{\rm p,\perp}$.[8] We now rewrite equations (1.1) and (1.4) as

$$f_\nu = \frac{D}{2c}\left(\frac{1-\beta}{\beta}\right)(\theta_{2x}^2 + \theta_{2y}^2) \tag{1.5}$$

$$f_t = \frac{V_{\rm p,\perp}}{\lambda\beta}\theta_{2x}. \tag{1.6}$$

Finally, we consider interference between points along the $\hat{\boldsymbol{x}}$ axis of the image ($\theta_{2y} = 0$) and the origin, and combine the expressions for f_ν and f_t, yielding

$$f_\nu = \eta f_t^2, \tag{1.7}$$

where we have defined

$$\eta \equiv \frac{D\lambda^2}{2cV_{\rm p,\perp}^2}\left(\frac{\beta}{1-\beta}\right). \tag{1.8}$$

[6] The effective velocity is the apparent velocity of the pulsar image through the scattering screen. It is a combination of the velocities of the three components of the system, the transverse velocity of the pulsar, $\boldsymbol{V}_{\rm p,\perp}$, the orbital velocity of the Earth, $\boldsymbol{V}_{\rm obs,\perp}$, and the velocity of the scattering screen, $\boldsymbol{V}_{\rm screen,\perp}$, with each velocity weighted by the distance from the screen.

[7] Note that, due to the θ^2 terms in equation (1.1), the secondary spectrum does not contain information about the sign of the θ_y component of image coordinates.

[8] The velocity of the Earth is only a factor of 10 smaller than the pulsar velocity in typical observations, so this approximation introduces measurable uncertainty. We use it because it works well and simplifies the analysis significantly. However, particularly for slow pulsars and screen placements near the observer ($\beta \gtrsim 0.5$), there is substantial change in $V_{\rm eff,\perp}$ over the course of the year due to the orbital motion of the Earth.

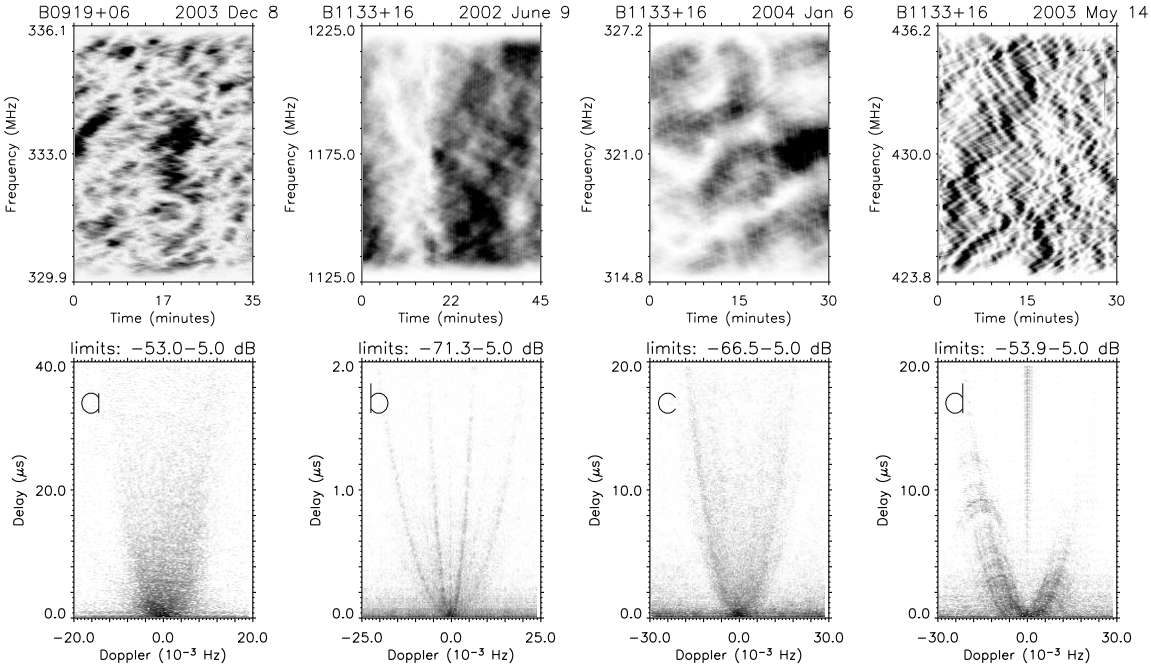

Figure 1.5: Examples of dynamic spectra (*top*) and secondary spectra (*bottom*) with a variety of types of scintillation arcs. Panel *a* shows a relatively simple example, in which a single parabola bounds most of the power in the secondary spectrum. Panels *b*–*d* depict PSR B1133 + 16 at three different epochs. (Although the observing frequencies shown vary, the character of the secondary spectra is comparable at any given epoch across a wide range of frequencies.) In panels *b* and *c*, two sharply defined arcs are present. In panel *d* (taken 11 months after panel *b* and 7 months before panel *c*), there are a number of inverted arcs, or *arclets*, with vertices along the primary arc.

Interference between points not along the $\hat{\boldsymbol{x}}$ axis will add a $\theta_{2y}^2 > 0$ term to equation (1.7). Therefore, equation (1.7) defines a parabola which bounds the power in the secondary spectrum; in this simple model, no power is allowed where $|f_\nu| < f_t^2$. These features, first identified by the Oberlin group (Becker, 2001; Kramer, 2001; Stinebring et al., 2001), are known as *scintillation arcs*.

We emphasize that the parabolic relationship between f_ν and f_t is simply a consequence of the $f_\nu \propto \theta^2$ scaling of the differential time delay (equation 1.1) and the $f_t \propto \theta$ scaling of the differential Doppler shift (equation 1.4); scintillation arcs are general products of scattering. Therefore, the presence of a single, sharply defined scintillation arc (e.g. Figure 1.3, 1.5*a*) indicates that the scattering is dominated by a thin screen; if a large portion of the scattering occured in the extended medium, the curvature parameter η would vary, washing out the sharp arc.

Previous observational work has explored several features of simple scintillation arcs; several examples are shown in Figure 1.5. Stinebring et al. (2004) and Becker (2001) show that scintillation

arcs are common—they have been observed in all 12 of the brighest pulsars visible from the Arecibo Observatory—and that the arc curvature for a given pulsar is constant over 20 years or more. Hill et al. (2003) show that arcs are present for a given pulsar at a given epoch over a factor of 3 or more in frequency, and that the arc curvature parameter scales as $\eta \propto \lambda^2$, as predicted by equation (1.8). Although only one arc is present in most observations, there are occasions on which two or more arcs are visible for a given pulsar (see Figure 1.5*b*, *c*), most likely indicating the presence of multiple thin scattering screens along the line of sight.

Numerous observations have multiple inverted arcs with vertices along the 'primary' arc (the arc with a vertex at $(f_t, f_\nu) = (0, 0)$, defined by equation 1.7). These *arclets* typically have the same curvature as the primary arc ($\eta' = -|\eta|$) (see Figure 1.5*d*).

For all the pulsars we have studied, the underlying curvature of the primary arc is unchanged over 20 years. Additional arcs are present at some epochs for some pulsars, as are arclets. However, these features are relatively transient; they are known to persist on timescales of days, but come and go over timescales of years. In this thesis, we use a new set of Arecibo data to improve our understanding of arclets. We seek to determine the timescale for which arclets persist. We extend the simple model presented above to explore an image geometry consisting of numerous hot spots displaced from the origin, which allows us to invert secondary spectra to image the scattering screen. Secondary spectra thus allow a single dish radio telescope to act as an interferometer with an angular resolution of order milliarcseconds.

Chapter 2

Scattering

In this chapter, we discuss the effects of the ionized component of the interstellar medium (IISM) on propagating radio waves.

2.1 Dispersion

The simplest effect of radio wave propagation through the IISM is *dispersion*. We follow the discussion in Lyne & Graham-Smith (1990, section 3.2). Pulsed radio waves of wavelength λ travel at the group velocity (Appendix B),

$$v_g = c\left(1 - \frac{n_\mathrm{e} r_0 \lambda^2}{2\pi}\right), \tag{2.1}$$

where c is the speed of light in a vacuum, n_e is the electron density and $r_0 = q_e^2/(m_e c^2) = 2.81 \times 10^{-13}$ cm is the classical electron radius. We consider the propagation of radio waves from a pulsar over a distance D, and treat the electron density as a function of distance, $n_\mathrm{e}(z)$. A wave passing a small distance $\mathrm{d}z$ through the IISM is delayed by a time

$$\mathrm{d}t = \mathrm{d}z\left(\frac{1}{c} - \frac{1}{v_g(z)}\right)$$

compared with free space. In the interstellar medium, n_e is typically $\sim 10^{-3}$ cm^{-3}, so, for meter wavelengths (300 MHz), $n_\mathrm{e} r_0 \lambda^2 \ll 1$. Therefore, using the binomial theorem,

$$\mathrm{d}t \approx \frac{r_0 c}{2\pi}\,\nu^{-2}\,n_\mathrm{e}(z)\,\mathrm{d}z, \tag{2.2}$$

where $\nu = c/\lambda$ is the observing frequency. The *dispersion measure* is defined as the electron column density along the line of sight,

$$\mathrm{DM} \equiv \int_0^D n_\mathrm{e}(z)\,\mathrm{d}z, \tag{2.3}$$

which is typically expressed in units of pc cm^{-3}. Thus, the total dispersion delay (compared with free space) is

$$t = \frac{r_0 c}{2\pi} \frac{\mathrm{DM}}{\nu^2}. \tag{2.4}$$

For a typical pulsar observation at an observing frequency $\nu = 300$ MHz, DM ≈ 10 pc cm^{-3}, so the dispersion delay is $t \approx 0.5$ s; the difference in dispersion measure over a 25 MHz bandwidth is ≈ 0.1 s. Low frequency channels are delayed more than high frequency channels. The dispersion measure has been determined experimentally with a fractional uncertainty $\lesssim 10^{-3}$ for each of the well-studied pulsars we observe. The data from each frequency channel is shifted to remove the effects of dispersion. This process is called *dedispersion*.

The dispersion measure of a pulsar is a measure of only the total electron column density along the line of sight; it is independent of any inhomogeneities in the distribution of electrons or of turbulence in the IISM. Because models of the electron content of the galaxy along all lines of sight exist (Taylor & Cordes, 1993; Cordes & Lazio, 2002, 2003), dispersion measure provides an easily observable, if crude, estimate of the pulsar distance.

2.2 Refractive and Diffractive Scintillation

Electromagnetic radiation scatters as it propagates through an ionized medium. Inhomogeneities in the electron density lead to multi-path propagation, so ray bundles arrive at the observer with varying time delays and, hence, phase shifts. If the source of the radiation is a point source and either the source or the medium has a non-zero velocity relative to the observer, interference between the rays leads to fluctuations in the observed intensity of the source. This phenomenon is most familiar as the twinkling, or scintillation, of stars due to the Earth's turbulent ionosphere. Radio scintillation can be observed due to the ionized plasma contained in the solar wind, the gas flowing out of the corona of the sun. Radio waves also undergo scintillation as they pass through the IISM. Pulsar scintillation due to the IISM was first identified by Lyne & Rickett (1968).

Pulsar scintillation is usually divided into two regimes: *refractive* and *diffractive* scintillation. Refractive scintillation is due to relatively large scale inhomogeneities in the electron density distribution of the IISM. Diffraction is a dispersive effect caused by small scale turbulence.

Previous work leads us to consider a model in which the scattering is dominated by a thin scattering screen perpendicular to the line of sight. We explore this model following the treatments in Lyne & Graham-Smith (1990, chapter 17) and Clegg, Fey, & Lazio (1998). The average phase velocity of interstellar plasma is given by (Appendix B)

$$v_\phi = c\left(1 + \frac{r_0 n_\mathrm{e} \lambda^2}{2\pi}\right). \tag{2.5}$$

Note that $v_\phi > c$, meaning that the plasma acts as a *diverging* lens. As the wave passes through an

inhomogeneity of size a with an electron density fluctuation $\Delta n_{\rm e}$, the phase is advanced by a time

$$\begin{aligned} \delta\tau &= a\left(\frac{1}{c}-\frac{1}{v_\phi}\right) \\ &\approx \frac{a}{c}\left(\frac{\lambda^2 r_0 \Delta n_{\rm e}}{2\pi}\right). \end{aligned} \tag{2.6}$$

The phase shift of the resultant wave is then

$$\phi = (2\pi\nu)\delta\tau = \lambda r_0 a \Delta n_{\rm e}, \tag{2.7}$$

which is proportional to the column density (dispersion measure) contribution of the inhomogeneity, $a\Delta n_{\rm e}$.

We consider a screen of thickness L containing randomly distributed inhomogeneities of typical size a, with electron density $n_{\rm e}$. We assume that $n_{\rm e}$ is much greater than the surrounding electron density so we can ignore scattering outside these inhomogeneities. A ray passing through the screen will encounter approximately $N \equiv L/a$ inhomogeneities. Because the distribution of the refracting inhomogeneities is random, the phase difference between two rays taking independent paths through the screen is

$$\Phi \approx \sqrt{N}\phi = \sqrt{La}\lambda r_0 \Delta n_{\rm e}. \tag{2.8}$$

We now use geometric, or refractive, optics to describe the behavior of rays passing through a scattering region. Let $n_{\rm e}$ be a function of the position on the screen, $n_{\rm e} = n_{\rm e}(x)$. The geometric refraction angle due to a single scattering entity is (Born & Wolf, 1999, Chapter 3)

$$\begin{aligned} \theta_r(x) &= \frac{\lambda}{2\pi}\frac{{\rm d}\phi}{{\rm d}x} \\ &= \frac{a\lambda^2 r_0}{2\pi}\frac{{\rm d}n_{\rm e}}{{\rm d}x} \qquad (2.9) \\ &= \frac{\lambda^2 r_0 \Delta n_{\rm e}}{2\pi}. \qquad (2.10) \end{aligned}$$

Similarly, the total scattering angle due to the screen is

$$\begin{aligned} \theta_{\rm scatt}(x) &= \frac{\lambda}{2\pi}\frac{{\rm d}\Phi}{{\rm d}x} \\ &= \frac{\lambda^2 r_0 (La)^{1/2}}{2\pi}\frac{{\rm d}n_{\rm e}}{{\rm d}x} \qquad (2.11) \\ &= \frac{\lambda^2 r_0 \Delta n_{\rm e}}{2\pi}\left(\frac{L}{a}\right)^{1/2}. \qquad (2.12) \end{aligned}$$

This angle is the size of the scatter-broadened image of the pulsar. The physical size of an object on the screen with an angular size $\theta_{\rm scatt}$ is defined as the *refractive size scale*:

$$s_r \equiv z\theta_{\rm scatt} = \frac{z r_0 \lambda^2 \Delta n_{\rm e}}{2\pi}\left(\frac{L}{a}\right)^{1/2}, \tag{2.13}$$

where $z \equiv (1-\beta)D$ is the distance from the screen to the observer. The pulsar scans a new slice of the ISM when it moves by the size of the scatter-broadened image. This timescale is the *refractive time scale*,

$$\Delta t_r = \frac{s_r}{V_{\mathrm{p},\perp}(1-\beta)} = \frac{D r_0 \lambda^2 \Delta n_\mathrm{e}}{2\pi V_{\mathrm{p},\perp}} \left(\frac{L}{a}\right)^{1/2}, \tag{2.14}$$

where $V_{\mathrm{p},\perp}$ is the transverse velocity of the pulsar.

As an example, we estimate the refractive time scale of a typical pulsar at meter wavelengths. We consider the pulsar PSR B0834+06, which is located a distance $D = 0.72$ kpc (Cordes & Lazio, 2003) with a transverse velocity $V_{\mathrm{p},\perp} = 174$ km s^{-1} (Lyne, Anderson, & Salter, 1982). Using a fractional screen thickness of 0.01 and a scattering entity size $a \sim 0.1$ AU with $\Delta n_\mathrm{e} \sim 10^{-3}$, we obtain $\Delta t_r \sim 3$ days.

Observations separated by the refractive time scale probe an independent portion of the ISM. Therefore, if there is no large scale organization in the screen, scintillation observations are typically expected to change character on this time scale. The above estimate of Δt_r agrees well with empirical measurements for this pulsar. However, because our observations probe outside the core of the scatter-broadened image, they are sensitive to larger slices of the medium, so the timescale for change is longer. This point is discussed further in Chapter 3.

We now consider the effects of the thin screen on radio waves using diffraction theory. Turbulence in the scattering screen produces small scale inhomogeneities which collectively act like a diffraction grating, causing an interference pattern analogous to two-slit interference. If the separation of the 'slits' is d, then maxima in the interference pattern occur at angles ϕ satisfying

$$m\lambda = d \sin\phi, \tag{2.15}$$

where m is an integer. A radio telescope only observes a single point in the diffraction pattern, but the observer scans the pattern due to the transverse velocity of the pulsar. For small angles, $\phi \propto \lambda/d$, so the diffraction pattern spreads out with wavelength.

Diffractive effects correspond to relatively small, randomly distributed inhomogeneities and thus impose a random phase component on the propagating wave. The corresponding features in pulsar dynamic spectra are *scintles*, random intensity variations with decorrelation time scales of minutes at meter wavelengths.

In summary, large angular separations due to refraction give rise to high frequency fringing patterns in the dynamic spectrum. These features are expected to persist for the time it takes the pulsar to move by the width of the scatter-broadened image, of order days. Diffractive effects are due to small scale inhomogeneities within the core of the pulsar image and thus give rise to large interference features in the dynamic spectrum.

Figure 2.1 shows an example in which the superposition of these two effects is present. Diffractive scintles with decorrelation time scales of ~ 10 min and decorrelation frequency scales of ~ 5 MHz are overlayed with periodic fringing, sloping from low radio frequency to high over the length of the

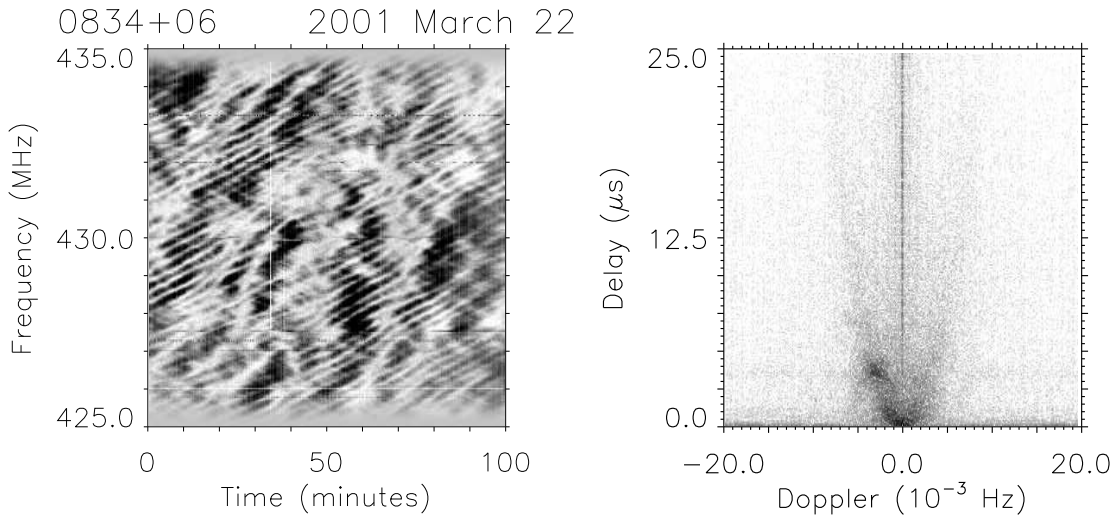

Figure 2.1: A dynamic (*left*) and secondary spectrum pair of PSR B0834+06. Note the fine periodic fringing pattern sloping from low frequency to high frequency with time. The intense region of the secondary spectrum at $f_t \approx -3$ mHz, $f_\nu \approx 4\,\mu$s corresponds to this fringing. The secondary spectrum has been truncated to show the detail; only regions with little power above the noise floor are not shown.

observation. The low Fourier frequency diffractive features are represented by the distribution of power near the origin of the secondary spectrum, while the high Fourier frequency fringe pattern is represented by an island of power at

$$(f_t, f_\nu) \approx (-3 \text{ mHz}, 4\,\mu\text{s}).$$

In contrast, the dynamic and secondary spectra in Figures 1.2 and 1.3 have little, if any, refractive component. The dynamic spectrum is dominated by diffractive scintles, and the secondary spectrum consists only of a single parabolic arc.

The primary arc is a diffractive effect; it arises due to interference between the diffraction-broadened pulsar image and the weak halo, which consists of rays diffracted through large angles. Organized, refractive effects can modify the diffractive model by (1) focusing or defocusing rays, contracting or expanding the image caused by random diffraction and (2) providing an alternative ray path which causes multiple imaging of the pulsar. Both of these cases are essentially lensing effects due to electron density inhomogeneities in the ISM. The former case only changes the size and intensity of the core of the image. However, the latter case puts a "hot spot," or region of enhanced intensity, in the image displaced from the geometrical position of the pulsar, which has the fringing effects in the dynamic spectrum described above.

Chapter 3

Arclets

Details in the secondary spectrum provide information about multi-component image geometries. The most common example of substructure in secondary spectra is what we call *arclets*: inverted arcs with vertices along the primary arc. In this chapter, we relate an image with multiple hot spots to the secondary spectrum. We then present observations which contain numerous arclets and discuss the properties of the corresponding image. In Chapter 4, we explore a possible physical model which explains the observed image geometry. Here, we focus only on the properties of the image.

3.1 Model

We first extend the model presented in Section 1.4 to consider interference between any two points in the image; that is, we do not fix $\boldsymbol{\theta}_1 = \mathbf{0}$. Rewriting equations (1.1) and (1.4),

$$f_\nu = \frac{D}{2c}\left(\frac{1-\beta}{\beta}\right)(\boldsymbol{\theta}_2^2 - \boldsymbol{\theta}_1^2) \tag{3.1}$$

$$f_t = \frac{1}{\lambda\beta}(\boldsymbol{\theta}_2 - \boldsymbol{\theta}_1)\cdot \boldsymbol{V}_{\mathrm{eff},\perp}. \tag{3.2}$$

To simplify the expressions, we define the dimensionless variables

$$p \equiv \boldsymbol{\theta}_2^2 - \boldsymbol{\theta}_1^2 = \frac{2c}{D}\left(\frac{\beta}{1-\beta}\right) f_\nu \tag{3.3}$$

and

$$q \equiv (\boldsymbol{\theta}_2 - \boldsymbol{\theta}_1)\cdot \hat{\boldsymbol{V}}_{\mathrm{eff},\perp} = \theta_{2x} - \theta_{1x} = \frac{\lambda\beta}{V_{\mathrm{eff},\perp}} f_t, \tag{3.4}$$

where $\hat{\boldsymbol{V}}_{\mathrm{eff},\perp}$ is a unit vector in the direction of $\boldsymbol{V}_{\mathrm{eff},\perp}$. Expanding,

$$\begin{aligned} p &= \theta_{2x}^2 + \theta_{2y}^2 - \theta_{1x}^2 - \theta_{1y}^2 \\ &= (\theta_{2x} - \theta_{1x})(\theta_{2x} + \theta_{1x}) + (\theta_{2y} - \theta_{1y})(\theta_{2y} + \theta_{1y}) \\ &= q(\theta_{2x} - \theta_{1x} + 2\theta_{1x}) + (\theta_{2y} - \theta_{1y})(\theta_{2y} + \theta_{1y}) \\ &= q(q + 2\theta_{1x}) + \theta_{2y}^2 - \theta_{1y}^2 \\ &= q^2 + 2\theta_{1x}q + (\theta_{2y}^2 - \theta_{1y}^2). \end{aligned} \tag{3.5}$$

Finally, rewriting using f_ν and f_t in terms of new constants and exploiting the symmetry of the secondary spectrum $P(f_\nu, f_t) = P(-f_\nu, -f_t)$,[1]

$$f_\nu = \pm\eta f_t^2 + \mathcal{A}\theta_{1x} f_t \pm \mathcal{B}(\theta_{2y}^2 - \theta_{1y}^2). \tag{3.6}$$

Combining the definitions of p and q with equation (3.5) and making the approximation $V_{\mathrm{eff},\perp} = (1-\beta)V_{\mathrm{p},\perp}$,

$$\eta = \frac{D\lambda^2}{2cV_{\mathrm{p},\perp}^2}\left(\frac{\beta}{1-\beta}\right) \tag{3.7}$$

$$\mathcal{A} = \frac{D\lambda}{cV_{p,\perp}} \tag{3.8}$$

$$\mathcal{B} = \frac{D}{2c}\left(\frac{1-\beta}{\beta}\right). \tag{3.9}$$

Note that η is the same as in equation (1.8); if we make the same assumptions as in Section 1.4.4 ($\boldsymbol{\theta}_1 = \mathbf{0}$ and $\theta_{2y} = 0$), equation (3.6) simplifies to equation (1.7), the primary parabolic arc. This derivation considers the arclet due to a region of intense power (a 'hot spot') in the image at an arbitrary position; the primary arc is a special (if common) case in which the hot spot is located at the geometrical position of the pulsar.

Equation (3.6) represents parabolic arcs with the same curvature as the primary arc and a translated vertex. Arclets have vertices along the primary arc if $\theta_{2y}^2 - \theta_{1y}^2 = 0$; that is, if the two points lie parallel to the velocity vector. For pairs of points not along the velocity vector but at small angular displacements, the offset term is negligible to first order in $\Delta\theta_y$. Therefore, this model predicts that most arclets lie near the primary arc if the variation in θ_y is small across the image, that is, if the image is elongated in a direction close to parallel to the pulsar velocity vector. Walker et al. (2004) present this result in a simulation in which an image is elongated along the θ_x axis; the resulting secondary spectrum consists of numerous arclets, each with the vertex along the primary arc.

[1] For the primary arc ($\theta_{1x} = \theta_{1y} = \theta_{2y} = 0$), this detail is irrelevant because we discard the redundant lower half plane, where $f_\nu = -\eta f_t$.

3.1.1 Arclet thickness

The thickness of an arclet due to a hot spot at coordinate $\boldsymbol{\theta}_2$ is determined by the size of the hot spot, $\Delta\boldsymbol{\theta}_2$, the size of the scatter-broadened image of the pulsar, $\Delta\boldsymbol{\theta}_1$, and the angular separation between the two relevant components of the image:

$$p = (\boldsymbol{\theta}_1 \pm \Delta\boldsymbol{\theta}_1)^2 - (\boldsymbol{\theta}_2 \pm \Delta\boldsymbol{\theta}_2)^2. \tag{3.10}$$

Arclets are typically ~ 30 dB below the peak intensity in the secondary spectrum (see below), so we assume that the angular size of the corresponding hot spot in the image is much smaller than the pulsar image itself. Therefore, we neglect second order terms in $\Delta\boldsymbol{\theta}_2$, yielding

$$p = \theta_1^2 \pm 2\theta_1\Delta\theta_1 + \theta_2^2 \pm 2\theta_2\Delta\theta_2 + \Delta\theta_1^2. \tag{3.11}$$

The pulsar coordinate $\theta_1 = 0$, which allows the simplification

$$p = \theta_2^2 \pm 2\theta_2\Delta\theta_2 + \Delta\theta_1^2, \tag{3.12}$$

giving an arclet thickness of

$$\begin{aligned} \Delta p = p_{\max} - p_{\min} &= (\theta_2^2 + 2\theta_2\Delta\theta_2 + \Delta\theta_1^2) - (\theta_2^2 - 2\theta_2\Delta\theta_2 + \Delta\theta_1^2) \\ &= 4\theta_2\Delta\theta_2. \end{aligned} \tag{3.13}$$

Using equation (3.3), this corresponds to

$$\Delta\theta_2 = \frac{2c}{D}\left(\frac{\beta}{1-\beta}\right)\frac{\Delta f_\nu}{4\theta_2}. \tag{3.14}$$

By equation (3.1), noting that $\boldsymbol{\theta}_1 = \mathbf{0}$, we can express the angular size in terms of the arclet size and coordinates in the secondary spectrum:

$$\Delta\theta_2 = \left(\frac{c\beta}{8Df_\nu(1-\beta)}\right)^{1/2}\Delta f_\nu. \tag{3.15}$$

3.2 Observations of Arclets

3.2.1 Archival data

We have seen evidence of arclets in Arecibo archival data from the 1980s (J. M. Cordes, private communication), as well as in our own observations from 1999–2003. Arclets are present in some observations of PSR B0823 + 26, PSR B0834 + 06, and PSR B1133 + 16 (see Hill et al., 2003). At other times, all of these pulsars exhibit sharply defined primary arcs with little substructure. For example, dynamic and secondary spectra of PSR B1133 + 16 taken every 1–3 months over a 6 month time period are shown in Figure 3.1. These data show an evolution from a fine diffraction

pattern in the dynamic spectrum and complicated structure in the secondary spectrum in 2003 July to a dynamic spectrum with little high frequency power and a sharply defined primary arc with no obvious substructure in 2004 January. In the intermediate observations, changes in the character of the dynamic spectrum are not obvious, but the amount of substructure in the secondary spectrum clearly wanes.

Our existing data do not have sufficient spectral resolution to detect arclets at high differential delays, so we cannot accurately determine the frequency at which arclets are present in observations or the time period over which they persist. However, we identify 12 epochs of observations of PSR B1133 + 16 and 12 epochs of observations of PSR B0834 + 06 separated by $\gtrsim$ 6 months. Of these epochs, arclets are observed in 4 for PSR B1133 + 16 and 3 epochs for PSR B0834 + 06.

3.2.2 Arecibo observations from 2004 January

During 2004 January, we had essentially daily observing runs at Arecibo over two one week time periods, separated by 10 days. We also had observations every 2–4 weeks in the preceding month and following 2 months. These data allow us to track substructure in secondary spectra over time scales ranging from one day to several months with excellent temporal resolution. During this time period, PSR B0834+06 had particularly rich structure, so we focused as much of our observing time

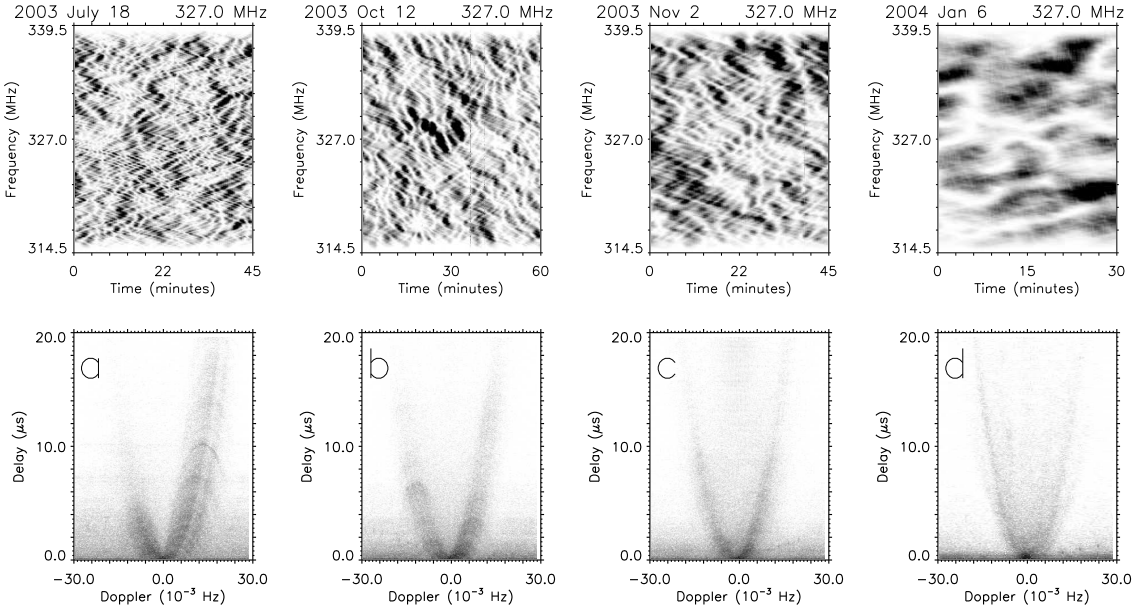

Figure 3.1: Dynamic and secondary spectra of PSR B1133 + 16 taken over a 6 month time period. Note the dramatic change in the character of both spectra.

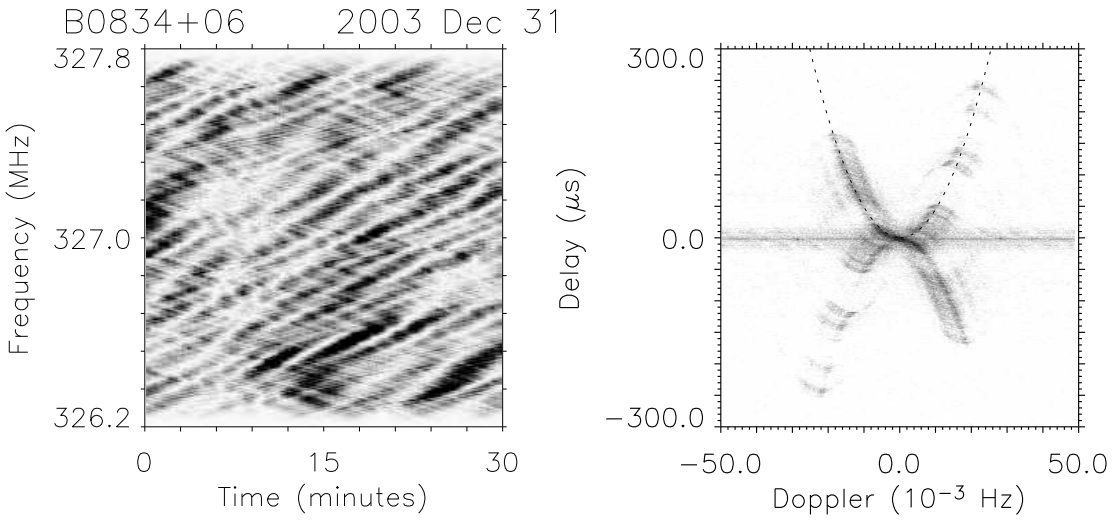

Figure 3.2: Dynamic and secondary spectra of PSR B0834 + 06 from 2004 Dec 31. Note the four distinct arclets at $|f_\nu| > 100\,\mu$s. The redundant lower half plane of the secondary spectrum is shown here to illustrate the fact that arclets are translations of the main arc. A parabola with curvature $\eta = 0.47$ s^3 is overplotted; note the position of the arclets relative to this primary arc.

as possible on this pulsar.

Typical observations of PSR B0834+06 lasted 30–60 min. We observed at multiple wavelengths, but focused on the 327 MHz band because previous observations have shown that substructure is most prominent at long wavelengths (see below). In most cases, we simultaneously collected data with a center frequency of ≈ 321 and ≈ 334 MHz to allow comparisons over a narrow wavelength range. A dynamic and secondary spectrum pair from one observation is shown in Figure 3.2; secondary spectra for observations near to 321 MHz are shown in Figure 3.3 over a 16 day period.

The maximum conjugate frequency and conjugate time are the Nyquist sampling limits, which are determined by the resolution in each dimension of the dynamic spectrum, the channel bandwidth and the integration time for each chunk:

$$\begin{aligned} f_{\mathrm{nyq},\nu} &= \frac{1}{2\,(\text{channel bandwidth})} \\ f_{\mathrm{nyq},t} &= \frac{1}{2\,(\text{chunk length})}. \end{aligned}$$

Any periodicities in the dynamic spectrum finer than these limits are not resolved. Therefore, in order to detect delays of $\approx 300\,\mu$s (which we see in these data) with a 1024 channel spectrometer, we must use a relatively small bandwidth of $\lesssim 1.5$ MHz.

3.2.3 Description of secondary spectra

The basic character of our 321 MHz observations of PSR B0834 + 06 remains essentially unchanged over 4 months of observing, as shown in Figure 3.3, although there are significant trends that are obvious over several days. Relatively near the origin of the secondary spectrum, the power is essentially contiguous, consisting of numerous, closely spaced arclets. The power distribution in the secondary spectrum is asymmetric; the contiguous power extends further on the left ($f_t < 0$) side of the spectra than on the right. The power distribution shifts from left to right over the course of the month of January: the extent of the power on the left side decreases steadily from Figure 3.3*c*–*m*, while the arclets on the right side move outward over time.

There are fine fringe patterns in the dynamic spectra, which are represented by isolated arclets at high differential delays and Doppler shifts in the upper right quadrant of the secondary spectrum. The vertices of the arclets lie along or slightly inside the bounding parabolic arc. Four distinct arclets are identifiable throughout the January data. These individual features persist for ≈ 30 days. Diffractive features normally persist for approximately the diffractive time scale, which is less than one day for these data. Therefore, the arclets cannot be individual, random diffractive features. The refractive time scale is ≈ 2.6 days, which is also much too small to explain these arclets. However, the refractive time scale corresponds to the time interval over which the pulsar moves by the width of the core of the image. Because our data probe the faint halo of the image, we expect refractive features to be detectable over a significantly longer time scale.

To investigate the distribution of power along the primary arc, we determine the total power in each of a collection of arclets, each with the same (absolute value of) curvature as the primary arc and with the vertex along the primary arc. The power in each arclet is plotted as a function of conjugate time (differential Doppler shift) in Figure 3.4 for four of the observations shown in Figure 3.3. In each of these plots, we have used a curvature parameter $\eta_{327\ \mathrm{MHz}} = 0.47\ \mathrm{s}^3$; we scale this to the appropriate frequency using the relation $\eta \propto \nu^{-2}$ (equation 3.7; see also Hill et al., 2003).

These cross-sectional cuts along the main arc allow us to easily pick out the coordinates of the vertices of arclets. From equation (3.6), we determine the coordinates of the vertices of arclets:

$$(f_\nu, f_t) = \left(\mp \frac{\mathcal{A}^2 \theta_{1x}^2}{4\eta} \pm \mathcal{B}(\theta_{2y}^2 - \theta_{1y}^2), \mp \frac{\mathcal{A}\theta_{1x}}{2\eta} \right). \tag{3.16}$$

Thus, from the f_t coordinate of the vertex of an arclet, we can determine the coordinate of the corresponding hot spot in the image, projected along the velocity vector. Therefore, the arc profile provides a partial image of the pulsar.[2] The position of a hot spot on the screen corresponding to an arclet with vertex f_t is

$$\theta_{1x} = -\frac{2\eta c V_{\mathrm{p},\perp} f_t}{D\lambda}. \tag{3.17}$$

[2]The secondary spectrum distorts intensities (Kramer, 2001; Reeves, 2003), so the arc profile indicates the position of hot spots in the image but does not directly indicate the relative intensity of hot spots.

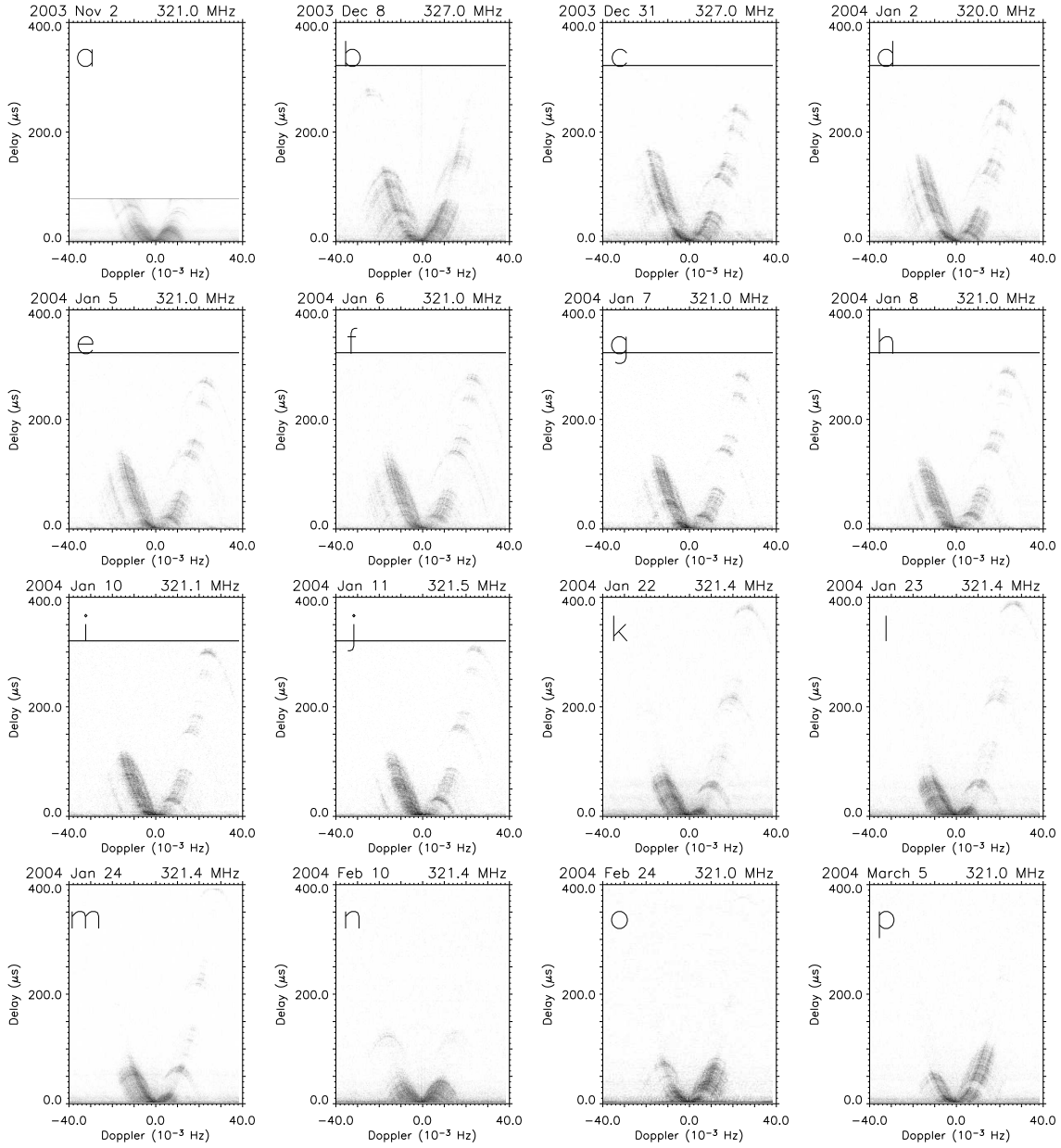

Figure 3.3: Secondary spectra for PSR B0834 + 06 from 2004 January. The axis scales have been fixed to simplify comparisons among plots; horizontal lines indicate the Nyquist frequency for the observation, above which there is no data.

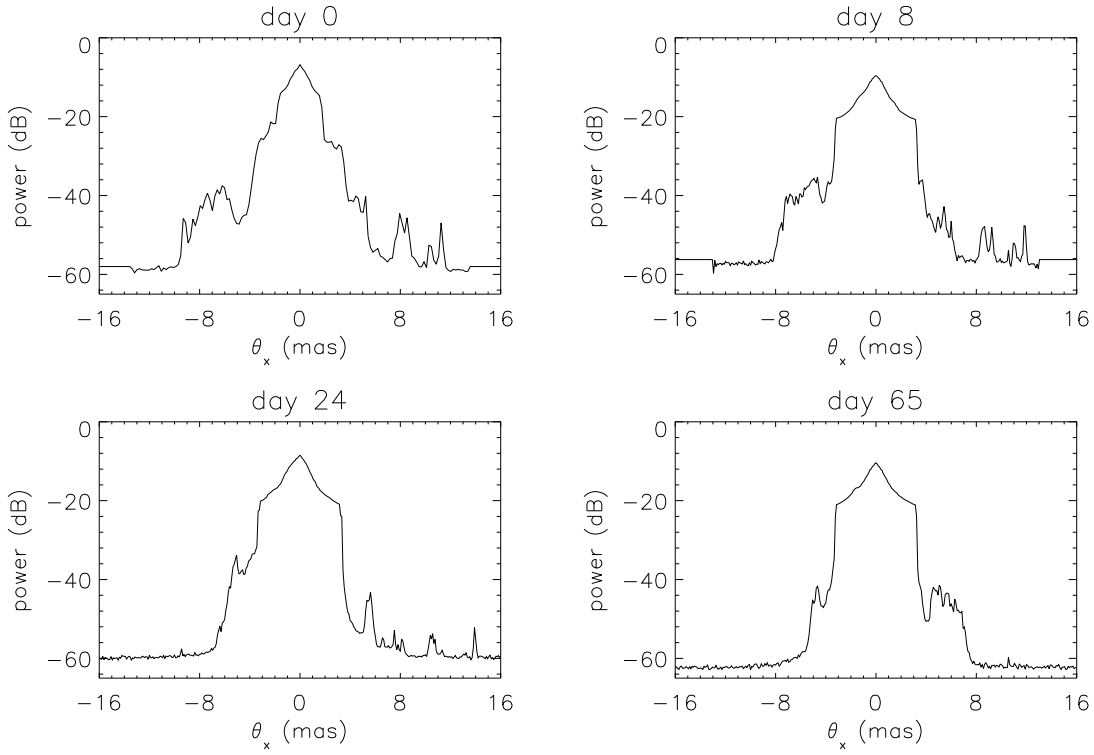

Figure 3.4: Power along a parabolic arc of curvature $\eta_{327\ \mathrm{MHz}} = 0.47\ \mathrm{s}^3$, summed over arclets with vertices along the main arc and curvature $-\eta$. These data correspond to panels *c*, *h*, *l*, and *p* of Figure 3.3, respectively. Day 1 corresponds to 2004 Jan 1.

For PSR B0834 + 06, $V_{\mathrm{p},\perp} = 174\ \mathrm{km\ s}^{-1}$ (Lyne et al., 1982) and $D = 0.72$ kpc (Cordes & Lazio, 2003). At an observing frequency of 321 MHz, we find $\eta = 0.47\ \mathrm{s}^3$, implying $\beta = 0.30$. A feature at, for example, $f_t = 30$ mHz corresponds to $\theta_x = 3.5 \times 10^{-8}$ rad = 7.3 mas. This corresponds to a size scale on the screen of $D(1-\beta)\theta_x = 3.6$ AU. This size scale is the displacement from the geometrical position of the pulsar of the scattering entity corresponding to the hot spot in the image.

These arclets typically have widths $\Delta f_\nu \sim 5$–$20\,\mu$s. Using equation (3.15), we find a typical angular size of $\Delta\theta \sim 0.2$ mas, which corresponds to a physical size of $a = D(1-\beta)\Delta\theta \sim 0.1$ AU. This result remains essentially consistent as the arclets move outward in f_ν over time. The angular size of the image of the scattering structure is an upper bound on the physical structure because a plasma overdensity is diverging; just as the image of the pulsar is broadened by diffractive effects, the image of the scattering structure may be enlarged.

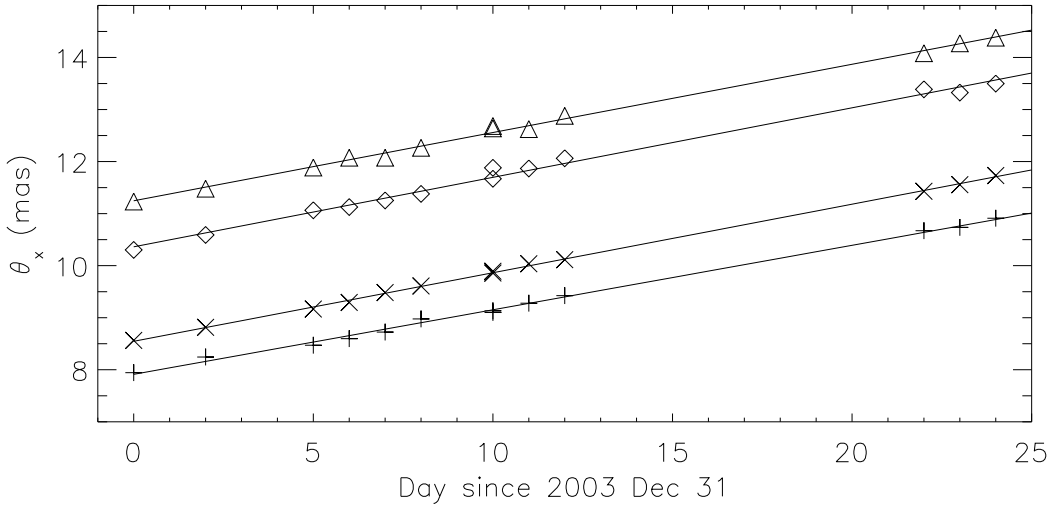

Figure 3.5: Position of four arclets over 25 days. Data were taken with observing frequencies from 320–327 MHz. Two parameter least-squares fits to a linear function are overplotted; the mean time derivative of the position of the arclets is $\dot{\theta}_x = 130 \pm 2$ μas day^{-1}. Day 1 corresponds to 2004 Jan 1, as in Fig. 3.4.

3.3 Screen Velocity

Although the thin screen model has been used for many years in discussions of scintillation, there have been no effective measurements of transverse velocities within the screen or of systematic screen movement. Some studies have made crude estimates of the velocity dispersion within the screen, and Clegg et al. (1998) estimate the velocity of a scattering entity based on the time it took to traverse the line of sight to a quasar (see Chapter 4). However, our data allow an unprecedented direct measurement of the systematic velocity of these scattering entities.

Figure 3.5 shows the image coordinate of the four isolated arclets in Figure 3.3 as a function of time. The features are first clearly identifiable on 2003 Dec 31; all four are present in all observations until 2004 Jan 24. The last remaining features fell below the noise between 2004 Jan 24 and 2004 Feb 10. All four features move linearly with time, at a mean rate of $\dot{\theta}_x = 130 \pm 2$ μas day^{-1}, corresponding to $D(1-\beta)\dot{\theta}_x = 113.4$ km s^{-1}. The velocity of the pulsar, projected onto the screen, is $V_{\mathrm{p},\perp}(1-\beta) = 120.8$ km s^{-1}. Therefore, the movement of the arclets relative to the pulsar is primarily due to the movement of the pulsar, implying that the scattering entities that give rise to the arclets are essentially static in the screen. There are a few plausible models for scattering entities that persist in a fixed location in the screen, which we explore in the following chapter.

The velocity of the scattering entities corresponding to arclets is 7 km s^{-1} smaller than the

velocity expected due to the pulsar proper motion alone. Until now, we have neglected the velocity of the Earth in our calculations based on the assumption that $V_{\mathrm{obs},\perp} \ll V_{\mathrm{p},\perp}$. However, the mean orbital speed of the Earth is $V_c = 29.8$ km s^{-1}, which could potentially account for some or all of the discrepancy between the arclet velocity and the pulsar velocity, projected onto the scattering screen.

Reeves (2003, ch. 6), following van de Kamp (1967), calculates the velocity of the pattern on the screen, considering the velocities of the pulsar and the observer over the course of the year. The components of the observer velocity in right ascension and declination[3] are

$$V_{\mathrm{obs},\alpha} = -ck\big[\cos\theta\cos\alpha\cos\odot + \sin\alpha\sin\odot\big] \tag{3.18}$$

$$V_{\mathrm{obs},\delta} = -ck\big[(\sin\epsilon\cos\delta - \cos\epsilon\sin\alpha\sin\delta)\cos\odot + \cos\alpha\sin\delta\sin\odot\big]. \tag{3.19}$$

where α and δ are the right ascension and declination of the source, $\theta = V_{\mathrm{obs},\perp}/c$ is the aberration angle, $\epsilon \approx 23.5°$ is the obliquity of the Earth's orbit, $\odot$ is the solar longitude, the angular distance the sun has traveled since the vernal equinox, and $ck = V_c(1-e^2)^{-1/2} = 30.31$ km s^{-1} is a constant term correcting for stellar aberration.

For PSR B0834 + 06, $V_{\mathrm{p},\alpha} = 2 \pm 5$ mas yr^{-1} and $V_{\mathrm{p},\delta} = 51 \pm 3$ mas yr^{-1} (Lyne et al., 1982). The celestial coordinates of this pulsar are $\alpha = 8^h37^m5.642^s$ and $\delta = 6°10'14.56''$. In mid-January, $\odot \approx 295°$, which yields $V_{\mathrm{obs},\alpha} = 6.82$ km s^{-1} and $V_{\mathrm{obs},\delta} = 173.9$ km s^{-1}. Applying the definition of $V_{\mathrm{eff},\perp}$ (equation 1.3),

$$V_{\mathrm{eff},\alpha} = (1-\beta)V_{\mathrm{p},\alpha} + \beta V_{\mathrm{obs},\alpha} = 13.40 \text{ km s}^{-1} \tag{3.20}$$

$$V_{\mathrm{eff},\delta} = (1-\beta)V_{\mathrm{p},\delta} + \beta V_{\mathrm{obs},\delta} = 119.89 \text{ km s}^{-1}. \tag{3.21}$$

The effective velocity of the pulsar, accounting for the orbital motion of the Earth, is $V_{\mathrm{eff},\perp} \approx 120.6$ km s^{-1} in January, only slightly smaller than the velocity we found by neglecting the orbital motion.

The apparent motion of the arclets is parallel to the $\boldsymbol{V}_{\mathrm{eff},\perp}$ vector; secondary spectra are not sensitive to the component of the arclet motion perpendicular to $\boldsymbol{V}_{\mathrm{eff},\perp}$. Therefore, the difference between $V_{\mathrm{eff},\perp}$ and the observed arclet velocity indicates that the transverse component of the velocity of the scattering entity is $\boldsymbol{V}_{\mathrm{screen},\perp} \cdot \hat{\boldsymbol{V}}_{\mathrm{eff},\perp} \approx -7$ km s^{-1}. The velocities of all four arclets are the same, within our uncertainties, implying that the corresponding scattering entities are either (1) essentially static within a comoving scattering screen or (2) multiple images of a single scattering entity.

The comoving scattering screen is consistent with a model in which the scattering screen is an expanding supernova shock front. These shock fronts can have velocities of ~ 100 km s^{-1}. The transverse velocity of a shock front is the expansion velocity only when the expansion is perpendicular

[3]Right ascension and declination are coordinates on the celestial sphere, similar to longitude and latitude, respectively.

to the line of sight; in that case, the front would appear elongated along the line of sight and would not act as a thin screen. However, if the expansion velocity is oblique to the line of sight, the front would act as a thin screen with non-zero transverse and radial components of the velocity. A transverse velocity of ~ 7 km s^{-1} seems consistent with this model.

3.4 Detectability of Arclets

Twenty years of pulsar scintillation observations at Arecibo and Green Bank, first presented in Becker (2001), show that scintillation arcs are observable in all 12 of the brightest pulsars visible at Arecibo and at least two additional pulsars observed in 1991-1992 with the Green Bank 140 foot telescope by R. Foster (private communication). Over the twenty year timescale, there is no significant variation in the curvature of the primary arc, implying that the scattering screen is a large structure moving slowly relative to D.[4] Because arclets have the same curvature as the primary arc, they must be caused by physical structures at the same distance as the scattering screen. However, there are dramatic changes in the "look and feel" of secondary spectra over time scales of ~ 6 months, as shown in Figure 3.1; arclets are present at some epochs, but not at others. Moreover, arclets have not been observed at all for several pulsars.

There are two natural explanations for the intermittent presence of arclets in secondary spectra. First, the scattering entities that cause arclets are present, but the resolution of the secondary spectrum is too coarse to detect them. This point is discussed below. Second, the scattering entities that cause arclets are not within the field of view of the secondary spectrum image. In this case, the frequency at which arclets occur could allow us to estimate the covering fraction of the scattering entities in the screen.

3.4.1 Resolution

Reeves (2003, chapter 3) derives the angular resolution of the secondary spectrum. On the conjugate time axis, the largest angle in the secondary spectrum corresponds to the Nyquist sampling limit, $(2\Delta t)^{-1}$, where Δt is time resolution of the dynamic spectrum. For this conjugate time, the observed angle is, from equation (3.4),

$$\theta_{x,\max} = \frac{\lambda\beta}{V_{\mathrm{eff},\perp}} f_t = \frac{\lambda\beta}{2\Delta t V_{\mathrm{eff},\perp}}.$$

The angular resolution in time is the maximum observed angle divided by half the number of time chunks in the dynamic spectrum, $T(2\Delta t)^{-1}$.

$$\theta_{x,\min} = \frac{\lambda\beta}{T V_{\mathrm{eff},\perp}}, \tag{3.22}$$

[4]The pulsar distance is so large that a motion of $0.01D$ over 20 yr for $D \sim 500$ pc would correspond to $V \sim 10^5$ km s^{-1} $\sim c$, so the essentially unchanging fractional distance to the scattering screen is not surprising.

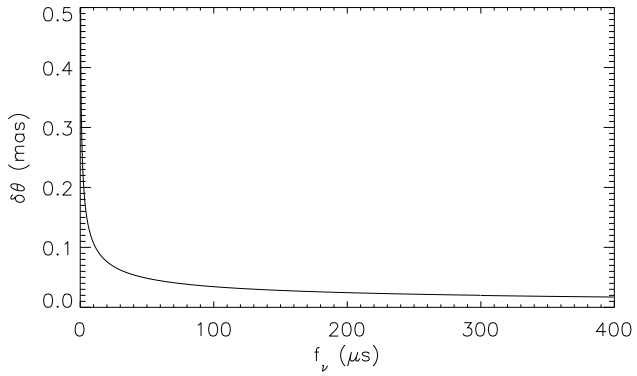

Figure 3.6: Angular resolution as a function of conjugate frequency for PSR B0834 + 06 with $B = 1.5625$ MHz.

where T is the observation length.

Because $f_\nu \propto \boldsymbol{\theta}^2$, the resolution, or step size, in f_ν changes with scattering angle. The Nyquist frequency is $f_{\nu,\max} = \mathrm{Nchans}(2B)^{-1}$ and the step size is $\delta f_\nu = B^{-1}$, where B is the bandwidth. The angular resolution in conjugate frequency is thus

$$\begin{aligned} \delta\theta &= \theta(f_\nu + \delta f_\nu) - \theta(f_\nu) \\ &= \sqrt{\frac{2c}{D}(f_\nu + \delta f_\nu)} - \sqrt{\frac{2cf_\nu}{D}} \\ &= \sqrt{\frac{2c}{D}}\left(\sqrt{f_\nu + \frac{1}{B}} - \sqrt{f_\nu}\right). \end{aligned} \tag{3.23}$$

This angular resolution is plotted in Figure 3.6. The angular resolution improves with scattering angle because $\theta \propto f_\nu^{1/2}$.

The angular resolution of observations of numerous pulsars, with typical observation lengths and bandwidths in the 327 MHz band, are shown in Table 3.1. These resolutions indicate that observations of all of these pulsars should all resolve structures of size $a \sim 0.1$ AU, the size of the structures we observe in PSR B0834 + 06. This implies that the lack of arclets in a secondary spectrum does indicate that no scattering entities with the properties discussed above are present in the screen.

The $\theta_{x,\min} \propto \lambda$ scaling of equation (3.22) shows that the angular resolution of secondary spectra is better at high observing frequencies than at low frequencies. This predicts that arclets should be more sharply defined at higher observing frequencies, as Hill et al. (2003) noted based on multi-frequency observations. However, our 2004 January observations indicate that substructure—particularly at high delays—is more prominent at low frequencies. This point is discussed in the

Pulsar	β	$V_{\mathrm{p},\perp}$ (km s^{-1})	D (kpc)	$\theta_{x,\mathrm{min},f_t}$ (mas)	$\theta_{\mathrm{min},f_\nu}$ (mas)	a_{min} (AU)	Ref.
B0823+26	0.32	191±6	0.37	0.088	0.048	0.032	*a*
B0919+06	0.60	500±80	1.21±0.19	0.063	0.026	0.076	*b*
B0834+06	0.30	170±20	0.72	0.090	0.034	0.065	*a*
B1133+16	0.58	630±40	0.35±0.02	0.048	0.049	0.017	*c*
B1929+10	0.37	163±5	0.331±0.010	0.12	0.050	0.049	*c*

Table 3.1: Observed parameters of several pulsars. Resolution angles correspond to a 60 min observation with $\Delta t = 10$ s at $\nu = 327$ MHz with $B = 1.5625$ MHz. The f_ν resolution is at $f_\nu = 100\,\mu$s. The minimum detectable size scale is $a_{\mathrm{min}} = D(1-\beta)\theta_{x,\mathrm{min}}$. Screen placements are from Reeves (2003).
References — (*a*) angular proper motion velocity from Lyne et al. (1982), distance estimated from DM by Cordes & Lazio (2003) (distance uncertainties $\sim$ 20–50%); (*b*) velocity and parallax distance measurement from Chatterjee et al. (2001); (*c*) velocity and parallax distance measurement from Brisken et al. (2002).

context of a plasma lens model in Chapter 4.

Chapter 4

Plasma Lenses and Extreme Scattering Events

The observed arclets which persist for at least 25 days at a fixed image position (moving only due to the velocity of the pulsar) indicate that some scattering structure of cross-sectional size $\lesssim 0.1$ AU is present in the screen. Because only turbulent plasma causes diffractive scattering, a small region of turbulence in an otherwise static region of the IISM could provide an appropriate scattering entity. However, this model requires an energy source to drive turbulence in a confined region.

Alternatively, gas clouds with a free electron overdensity (compared to the surrounding medium) can act as refractive lenses. Such lenses have been proposed as the scattering entities responsible for extreme scattering events (ESEs). ESEs, first observed by Fiedler et al. (1987), are seen in long term monitoring of the flux of quasars, which are bright, distant radio sources. When the line of sight to a quasar passes through a refracting cloud, the lens focuses or defocuses the radiation, causing dramatic changes in the observed intensity of the source. These clouds are proposed to have as much as Jovian mass ($\sim 10^{-3}\,M_{\odot}$, although the mass of the ionized component is much smaller) and $\sim$ AU size scales (Walker & Wardle, 1998).

In this chapter, we explore a model in which the electron clouds that are responsible for ESEs also cause the arclets in pulsar secondary spectra. Our data give us the ability to image multiple lenses in a single observation and to track the rays refracted by these lenses as the pulsar moves past them.

Quasars are comparatively large (~ 1 mas in angular size), so scintillation observations are not possible. Therefore, the effects of a plasma lens can only be observed if the quasar line of sight passes directly through the lens. Because pulsar scintillation observations probe angular scales of $\gtrsim 10$ mas, these data—if capable of detecting plasma lenses—provide a detection area ~ 100 times larger than that of quasar flux monitoring programs. Fiedler et al. (1994) summarize existing ESE

observations. In quasar monitoring programs of ~ 400 sources taken over an 11 yr period, 10 ESEs have been identified. In contrast, our scintillation observations have detected the same physical structures in one month of monitoring of 5 pulsars.

4.1 Plasma Lens Properties

Clegg, Fey, & Lazio (1998) present the refractive properties of plasma lenses. Following their discussion, we consider a plasma lens in the ISM where the column density $N_e \equiv a n_{\rm e}(x)$ (where, as before, a is the size of the lens and x is a position on the screen) follows a spherically symmetric Gaussian distribution. We now restate the scattering parameters from Section 2.2:

$$N_e(x) = N_0 e^{-(x/a)^2} \tag{4.1}$$

$$\phi(x) = \lambda r_0 N_0 e^{-(x/a)^2} \tag{4.2}$$

$$\theta_r = \frac{\theta_{\rm scatt}}{\sqrt{L/a}} = -\frac{\lambda^2 r_0 N_0 x}{\pi a^2} e^{-(x/a)^2}. \tag{4.3}$$

Here N_0 is the maximum column density, L is the screen thickness, ϕ is the phase shift imposed by the screen, θ_r is the refraction angle due to a single lens, and $\theta_{\rm scatt}$ is the refraction angle due to the screen. We now define dimensionless variables to simplify the above equations:

$$u \equiv x/a \tag{4.4}$$

is the dimensionless position on the screen and

$$\theta_l \equiv a/D_o \tag{4.5}$$

is the observed angular size of the lens, typically ≈ 0.1 mas for our arclets; $D_o = (1-\beta)D$ is the distance from the screen to the observer. Clegg et al. (1998) define a *scattering parameter*

$$\alpha \equiv \frac{\lambda^2 r_0 N_0 D_o}{\pi a^2}, \tag{4.6}$$

which gives

$$\frac{\theta_r(u)}{\theta_l} = -\alpha u e^{-u^2}. \tag{4.7}$$

The maximum possible refracting angle for the lens satisfies

$$0 = \frac{{\rm d}\theta_r}{{\rm d}u} = -e^{-u^2} + 2u^2 e^{-u^2},$$

implying $u = 2^{-1/2}$. Therefore, the characteristic refracting angle is

$$\frac{\theta_r}{\theta_l} = -\frac{\alpha}{\sqrt{2e}} \approx -0.43\,\alpha. \tag{4.8}$$

Arclet	min θ_x (mas)	max θ_x (mas)	α	N_0 (pc cm^{-3})	n_e (cm^{-3})
A	10.89	13.00	139	8E-5	171
B	11.71	13.95	149	9E-5	183
C	13.56	15.84	171	10E-5	210
D	14.40	16.62	180	11E-5	222

Table 4.1: Lower and upper bounds on maximum observed angular displacement of arclets from the pulsar, scattering parameter, peak column density, and peak electron density. Lower bound from maximum observed position of arclet (on day 24); upper bound from projected position of arclet on first observation for which the arclet was not observed (day 41). Scattering parameter α assumes a lens size $\theta_l = 0.2$ mas ($a = 0.1$ AU).

The scattering parameter α thus characterizes the maximum refracting angle possible due to the lens. Therefore, if we can observe a particular lens on frequent, successive observing runs and can see the power due to the lens drop below the noise floor, we can estimate α and the electron density of the lens.

All of the arclets we consider in observations of PSR B0834 + 06 during 2004 January were visible on day 24, and all fell below the noise floor by our next observation, on day 41. Therefore, the maximum refracting angle θ_r of each lens must be between the observed refracting angle on day 24 and the extrapolated refracting angle on day 41. These upper and lower bounds on θ_r for each arclet are shown in Table 4.1. We assume that θ_r is the mean of these two bounds. From this, we calculate the scattering parameter α (from equation 4.8), the peak electron column density, and the electron density $n_e = N_0/a$ of the plasma lens (from equation 4.6). In all cases, the column density contribution of the lens is small compared to the dispersion measure, DM = 12.89 pc cm^{-3} (Hobbs et al., 2003). Nonetheless, the fractional thickness of the lens is $aD^{-1} \sim 10^{-9}$, so the lens represents an electron overdensity of $\sim 10^4$ relative to the mean electron content along the line of sight to this pulsar.

From these parameters, we estimate the mass of the lens to be $M_l \sim n_e m_p a^3 = 1.1 \times 10^{15}$ g $= 6 \times 10^{-19}\, M_\odot$, where $m_p = 1.7 \times 10^{-24}$ g is the mass of the proton. These values agree well with the parameters derived for an ESE along the line of sight to the quasar 1741–038: $a = 0.065$ AU, $n_e \sim 300$ cm^{-3} and $M_l \sim 8 \times 10^{-19}\, M_\odot$ (Clegg et al., 1998). Other ESEs have been associated with lenses with electron densities as much as 2 orders of magnitude larger than these values (Clegg et al., 1998; Walker & Wardle, 1998). These mass parameters pertain only to the ionized component of the lens.

4.1.1 Refractive geometry of Gaussian lenses

In the above discussion, we implicitly assumed that the four arclets each correspond to a distinct physical lens. However, we note the possibility that these are in fact multiple images due to a single

lens (or two lenses). Clegg et al. (1998) discuss the refractive properties of Gaussian plasma lenses; we summarize their discussion here. Their Figure 2 is a schematic diagram of the refractive behavior. There are three regions of interest, which depend upon the position of the observer relative to the lens axis and the distance from the lens.

Near the lens axis is the defocusing region. In this relatively simple case, the diverging lens spreads out the rays, which decreases the source brightness. However, the geometry of the lens is unchanged; no ray crossings occur. Further from the lens axis but relatively near to the pulsar is a focusing region. Here, the rays converge, but no ray crossings occur. Therefore, the lens increases the source brightness and shifts the apparent position of the source but does not distort the geometry. Further from the lens, rays do cross. Ray bundles thus appear to come from different angles, causing multiple images to be visible. The different ray bundles do not necessarily have the same number density or intensity.

In this work, we do not attempt to determine the position of the observer with respect to these regions.

4.2 Comparison to Previous Observations

We conclude by comparing the lens structures identified in our observations with previously observed lenses, in connection with both ESEs and pulsar scintillation.

Clegg, Fiedler, & Cordes (1993) report on observations of PSR B0823 + 26 with discontinuities in the dynamic spectrum on timescales of ~ 2 min. The discontinuities coincide with a significant change in the flux density of the pulsar. They identify these discontinuities with strong refraction in the ISM; they propose that the discontinuities occur when the observer passes through a caustic, which corresponds to a dramatic increase in the pulsar flux density. This process is identical to that which is thought to cause ESEs, and they derive lens properties that agree with this work and Clegg et al. (1998). They do not use the secondary spectrum analysis, so their information about the image is less detailed than that presented for PSR B0834 + 06in this work. We have access to observations of the same pulsar from 1991 (A. Clegg, private communication), but have not attempted to invert these data.

Rickett, Lyne, & Gupta (1997) report on observations of PSR B0834 + 06 in 1984 Sept. They identify an episode of periodic fringing in the dynamic spectrum with an island of power at a high differential delay in the secondary spectrum. This island of power is different from arclets in that its vertex is well within the primary arc—the differential Doppler shift is small. It corresponds to a single refractive hot spot in the image that does not lie along the pulsar velocity vector. Our data contain no evidence of arclets so significantly displaced from the primary arc. Analysis of data like these—and the rarity of these types of arclets—could allow us to estimate the sensitivity of secondary spectra to lenses displaced from the pulsar propagation path.

Walker & Wardle (1998) propose that lenses are an ionized "skin" surrounding a cool (non-ionized) self-gravitating cloud of $\sim$ Jovian mass ($\sim 10^{-3}\,M_{\odot}$). These clouds could account for a large fraction of the mass of the Galaxy, and would be extremely difficult to detect without the ionized tracer.

Arclet analysis allows a reasonably accurate and independent distance determination, whereas Clegg et al. (1998) must infer the position of the lens by associating it with known structures. In particular, the curvature of the arclet shows that it is located at the same position of the screen (which is present in over twenty years of observations). The association of the lens with the screen is not an inference but a requirement of our data.

Chapter 5

Conclusions

5.1 Summary

In this thesis, we have used pulsar scintillation observations to probe the ionized component of the interstellar medium (IISM) on AU size scales. Previous work had shown that the presence of scintillation arcs in pulsar secondary spectra requires that the scattering along the line of sight to the pulsar is dominated by a thin screen of scattering material. An isotropic image gives rise to a sharply delineated arc, while an anisotropic image with refractive "hot spots" elongated along the pulsar velocity vector gives rise to detailed substructure and arclets in the secondary spectrum (Walker et al., 2004). The elongated image implies a preferential alignment directionality in the screen, most likely implying the presence of a magnetic field (Higdon, 1984, 1986).

Twenty-five years of archival scintillation data from the Arecibo Observatory show that arclets are present in $\sim 25\%$ of low radio frequency observations of PSR B0834 + 06 and PSR B1133 + 16, and that the decorrelation time scale of substructure is $\sim$ 6 months. In an intensive observing campaign at Arecibo, we sought to track this substructure on a daily, weekly, and monthly basis in order to better understand the mechanisms that cause arclets.

Secondary spectra of PSR B0834+06 suited our purposes ideally in 2004 January (see Figure 3.3. Of particular interest were four isolated arclets at high delays. These arclets were present throughout a month of observations, and their angular separation from the pulsar changed over the course of the month in a linear fashion, as shown in Figure 3.5. This transverse motion is dominated by the velocity of the pulsar and implies a screen velocity of 7 km s^{-1}.

We applied a plasma lens model (Clegg, Fey, & Lazio, 1998) to our observations, assuming that the high delay arclets are caused by refracting plasma lenses in the scattering screen. We place an upper bound of $a \sim 0.1$ AU on the lens size and estimate an electron density within the lens of $n_e \sim 200$ cm^{-3}. The ionized component of the lens thus has a mass of $M_l \sim 10^{-18}\, M_\odot$; if the lens is an ionized skin surrounding a neutral cloud, there may be a considerably larger mass associated with

the lens (Walker & Wardle, 1998). These parameters are very similar to the predicted parameters for the plasma lenses thought to cause Extreme Scattering Events (ESEs) in quasars.

The connection between ESEs and the refractive lenses observed in our data is exciting. ESEs are poorly understood, largely because they are detected only rarely in very long term monitoring programs of hundreds of quasars. In contrast, the compact angular size of pulsars allows scintillation observations, which provides a much larger field of view for detecting these lenses. The high transverse velocity of pulsars means that they cover a large region of the screen in a relatively short time period. Quasars are so distant that they have a transverse angular velocity of zero, so the relevant time scale is defined by the velocity of the slowly moving lens. Pulsar scintillation thus provides an excellent tool for investigating the physical properties and spatial distribution of these lenses.

5.2 Future Work

Future observations will seek to resolve the frequency at which arclets are present in pulsar secondary spectra and, thus, the spatial distribution of plasma lenses. However, much progress can be made with existing data.

The flux density of our dynamic spectra are uncalibrated, although we have calibration information. With calibrated intensity information, we can analyze pulsar light curves (total intensity as a function of time), both over the course of a ~ 60 min observation and over the course of several days, and compare them to ESE light curves (see Clegg, Fiedler, & Cordes, 1993). However, we expect that the modulation in pulsar flux density will be small because the lenses are not necessarily obscuring the line of sight to the pulsar.

The physical origins of both the scattering screen and the plasma lenses remain unknown. Scintillation arcs, in combination with pulsar distances, provide an accurate distance measurement to the scattering screen. These screen locations can be compared to known structures, such as expanding supernova shock fronts and the edge of the Local Bubble.

We have obtained code which simulates radio wave propagation from a coherent source through one or many phase-changing screens from T. J. W. Lazio (2003, private communication). We are modifying this code to create simulated dynamic spectra due to screens with known scattering properties. With this simulation, we will be able to explore the effects of multiple screens, including the limit of scattering in an extended medium.

A simpler simulation code generates secondary from an assumed image geometry (Reeves, 2003; Walker et al., 2004). This code has proven useful in developing our understanding of scintillation arcs and can be used to further analyze the effects of anisotropy in the image on substructure in the secondary spectra.

Lastly, the plasma lens can be used to peer into the emission region of the pulsar magnetosphere, which is not well understood (Cordes, Weisberg, & Boriakoff, 1983). Rays emitted from opposite sides over the emission region and refracted through the lens travel through different path lengths,

resulting in a path length difference and, thus a phase delay. This phase delay is $\lesssim 1$ radian (Wolszczan & Cordes, 1987), so we do not expect any phase wrapping. In computing the secondary spectrum, we normally discard the phase information in the Fourier transform, but this information is relevant for considering these small phase differences. In creating dynamic spectra, we typically total power over the entire pulse. The pulse profile can be divided into multiple components, which correspond to different regions of the rotating emission region. With information about the phase delay between pulse components, we can estimate the size of the emission region and investigate the emission across the magnetosphere, in order to improve our understanding of neutron stars.

Appendix A

Path Length of Scattered Rays

We calculate the path length difference between two rays with observed angles θ_1 and θ_2. We use the symbols defined in Section 1.4 and Figure 1.4. The propagation path length of one ray is

$$\mathcal{L} = \frac{D_s}{\cos\theta_0} + \frac{D - D_s}{\cos\theta}. \tag{A.1}$$

Using small angle approximations and the binomial theorem,

$$\begin{aligned} \mathcal{L} &= D_s\left(1 + \frac{\theta_0^2}{2}\right) + (D - D_s)\left(1 + \frac{\theta^2}{2}\right) \\ &= (D - D_s)\frac{\theta^2}{2} + D_s\frac{\theta_0^2}{2} + D. \end{aligned}$$

Note that $D_s \tan\theta_0 = (D - D_s)\tan\theta$, so $D_s\theta_0 = (D - D_s)\theta$ for small angles. Thus,

$$\begin{aligned} \mathcal{L} &= \frac{\theta^2}{2}\left(D - D_s + D_s\left(\frac{D - D_s}{D_s}\right)^2\right) + D \\ &= \frac{\theta^2}{2}(D - D_s)\frac{D}{D_s} + D \\ &= \frac{D\theta^2}{2}\left(\frac{1-\beta}{\beta}\right) + D, \end{aligned} \tag{A.2}$$

where $\beta \equiv D_s/D$. The path length difference is therefore

$$\Delta\mathcal{L} = \mathcal{L}_2 - \mathcal{L}_1 = \frac{D}{2}\left(\frac{1-\beta}{\beta}\right)(\theta_2^2 - \theta_1^2). \tag{A.3}$$

Appendix B

Radio Wave Propagation in Plasma

We derive the conditions under which a radio wave can propagate through a plasma and the phase and group velocities of radio waves in the plasma. We consider the effects of the electric field of the radiation on electrons, following Weisstein (2004). The electrostatic force on a single electron is given by

$$m_e \ddot{\boldsymbol{r}} = q_e \boldsymbol{E}, \tag{B.1}$$

where m_e is the mass of the electron, $\boldsymbol{r}$ is the position of the electron, $-q_e$ is the charge of the electron, and $\boldsymbol{E}$ is the electric field. The moving charges form a current density given by

$$\boldsymbol{J} = n_\mathrm{e} q_e \dot{\boldsymbol{r}},$$

where n_e is the number density of electrons. Differentiating,

$$\frac{\partial \boldsymbol{J}}{\partial t} = n_\mathrm{e} q_e \ddot{\boldsymbol{r}} = \frac{n_\mathrm{e} q_e^2}{m_e} \boldsymbol{E}. \tag{B.2}$$

We wish to consider the effect of the electric field of a radio wave on the free electrons in the plasma. The electric field of a plane wave is

$$\boldsymbol{E} = E_0 e^{i(kz - \omega t)} \hat{\boldsymbol{x}},$$

where $\hat{\boldsymbol{x}}$ is a unit vector pointing in the direction of the electric field, z is the coordinate in the propagation direction, k is the wave number, ω is the angular frequency of the wave, and E_0 is the amplitude of the electric field. Thus,

$$\nabla^2 \boldsymbol{E} = -k^2 \boldsymbol{E} \tag{B.3}$$

$$\frac{\partial^2 \boldsymbol{E}}{\partial t^2} = \omega^2 \boldsymbol{E}. \tag{B.4}$$

The wave equation for a conductor is (Griffiths, 1999, p. 394)

$$\nabla^2 \boldsymbol{E} = \frac{1}{c^2}\frac{\partial^2 \boldsymbol{E}}{\partial t^2} + \mu \frac{\partial \boldsymbol{J}}{\partial t}, \tag{B.5}$$

where $\mu = (\epsilon c^2)^{-1} \approx (\epsilon_0 c^2)^{-1}$ is the permeability of the medium. Substituting equations (B.2—B.4) into equation (B.5), we obtain

$$\boldsymbol{E}\left[-k^2 + \frac{\omega^2}{c^2} - \frac{1}{\epsilon_0 c^2}\frac{n_\mathrm{e} q_e^2}{m_e}\right] = \boldsymbol{0} \tag{B.6}$$

Solving for the phase velocity,

$$v_\phi^2 \equiv \frac{\omega^2}{k^2} = c^2\left(1 - \frac{n_\mathrm{e} q_e^2}{\epsilon_0 m_e \omega^2}\right)^{-1}. \tag{B.7}$$

In order for a radio wave to propagate through the plasma, the phase velocity must be real, which requires

$$\frac{n_\mathrm{e} q_e^2}{\epsilon_0 m_e \omega^2} < 1.$$

The minimum frequency that meets this condition is called the *plasma frequency*, ω_e. Customarily expressed in terms of $e^2 = q_e^2(4\pi\epsilon_0)^{-1}$,

$$\omega_e^2 \equiv \frac{4\pi n_\mathrm{e} e^2}{m_e}. \tag{B.8}$$

The plasma frequency is the frequency at which a group of electrons will oscillate if displaced from their equilibrium position (Feynman, Leighton, & Sands, 1964; Krall & Trivelpiece, 1973).

The phase velocity is often expressed as $v_\phi = c/n_r$, where n_r is the index of refraction. From equation (B.7),

$$n_r = \sqrt{1 - \frac{\omega_e^2}{\omega^2}}.$$

For $n_\mathrm{e} = 10^{-3}$ cm^{-3}, as is typical for the IISM, $\omega_e \sim 1$ Hz. Even for a region where n_e is several orders of magnitude higher than the typical values, $\omega_e \ll \omega$ for radio frequencies $\gtrsim 300$ MHz. Therefore, we use the binomial theorem to find

$$\begin{aligned} n_r &\approx 1 - \frac{\omega_e^2}{2\omega^2} \\ &= 1 - \frac{r_0 n_\mathrm{e} \lambda^2}{2\pi}. \end{aligned} \tag{B.9}$$

The phase velocity is then

$$v_\phi = \frac{c}{n_r} = c\left(1 + \frac{r_0 n_\mathrm{e} \lambda^2}{2\pi}\right). \tag{B.10}$$

The group velocity of the wave is

$$v_g = \frac{\partial \omega}{\partial k}. \tag{B.11}$$

Solving equation (B.7) for ω and differentiating,

$$\frac{\partial \omega}{\partial k} = c\left(1 + \frac{4\pi n_{\mathrm{e}} e^2}{m_e \omega^2}\right)^{-1/2}.$$

Substituting $\omega = 2\pi c/\lambda$ and again using the binomial theorem, we find

$$v_g = c\left(1 - \frac{r_0 n_{\mathrm{e}} \lambda^2}{2\pi}\right). \tag{B.12}$$

The phase velocity is the velocity at which individual wavefronts propagate; it is always greater than c in a plasma. The group velocity is the propagation velocity of wave packets; $v_g < c$ in a plasma.

Appendix C

Glossary of Notation

This appendix lists the symbols used throughout this work, and definitions where relevant. Boldface symbols denote vectors (e. g. $\boldsymbol{V}_{\mathrm{eff},\perp}$), with $V_{\mathrm{eff},\perp} = |\boldsymbol{V}_{\mathrm{eff},\perp}|$.

Symbol	Units	Description
		Physical constants
$r_0 = q_e^2/(m_e c^2)^{-1}$	cm	classical electron radius (2.81×10^{-13} cm)
		Electromagnetic radiation
λ	m	wavelength
ν	MHz	radio frequency
$n_r = 1 - \frac{\lambda^2 r_0 n_e}{2\pi}$		index of refraction of plasma
v_g	m s^{-1}	group velocity
$v_\phi = c/n_r$	m s^{-1}	phase velocity
$\phi = \lambda r_0 a \Delta n_\mathrm{e}$	rad	phase shift of wave in electron density inhomogeneity in ISM
		Image Angles
$\boldsymbol{\theta} = \theta_x \hat{\boldsymbol{x}} + \theta_y \hat{\boldsymbol{y}}$	mas	observed angle from geometrical position of the pulsar
$\boldsymbol{\theta}_0$	mas	emitted angle of a ray observed at angle $\boldsymbol{\theta}$
$\boldsymbol{\theta}_\mathrm{scatt} = \boldsymbol{\theta}_p - \boldsymbol{\theta}_0$	mas	scattering angle
		Distances
D	kpc	distance from the pulsar to the observer
D_s	kpc	distance from the pulsar to the scattering screen
$D_0 = D - D_s$	kpc	distance from the screen to the observer
$\beta = D_s/D$		fractional distance of the screen from the pulsar to the observer

Symbol	Units	Description
		Velocities
$\boldsymbol{V}_{\mathrm{p},\perp}$	km s^{-1}	pulsar velocity (transverse component)
$\boldsymbol{V}_{\mathrm{obs},\perp}$	km s^{-1}	observer velocity (transverse component)
$\boldsymbol{V}_{\mathrm{screen},\perp}$	km s^{-1}	screen velocity (transverse component)
$\boldsymbol{V}_{\mathrm{eff},\perp}$	km s^{-1}	effective velocity ($= (1-\beta)\boldsymbol{V}_{\mathrm{p},\perp} + \beta\boldsymbol{V}_{\mathrm{obs},\perp} + \boldsymbol{V}_{\mathrm{screen},\perp}$)
		Dynamic and secondary spectra
$S(\nu, t)$	Jy	dynamic spectrum
$P(f_\nu, f_t) = \lvert\tilde{S}(\nu,t)\rvert^2$	dB	secondary spectrum, or power spectrum of the dynamic spectrum
f_ν	μs	conjugate frequency, or differential time delay
f_t	mHz	conjugate time, or differential Doppler shift
$p = \boldsymbol{\theta}_2^2 - \boldsymbol{\theta}_1^2$	(mas)^2	dimensionless conjugate frequency
$q = \theta_{2x} - \theta_{1x}$	mas	dimensionless conjugate time
$\eta = \frac{D\lambda^2}{2cV_{\mathrm{p},\perp}^2}\left(\frac{\beta}{1-\beta}\right)$	s^3	arc curvature parameter ($f_\nu = \eta f_t^2$)
		ISM and plasma lenses
n_{e}	cm^{-3}	electron number density
DM	pc cm^{-3}	*dispersion measure*; total electron column density from the pulsar to the observer
N	pc cm^{-3}	electron column density of plasma lens
a	AU	size of scattering entity (or inhomogeneity, or plasma lens)
L	AU	thickness of screen
$\theta_l = a/D_0$	mas	observed angular size of lens
$\theta_r = \theta_{\mathrm{scatt}}(d/a)^{-1/2}$	mas	refraction angle due to a single lens
$\alpha = \frac{\lambda^2 r_0 N D_0}{\pi a^2}$		scattering parameter of lens

Bibliography

Becker, K. M. 2001, Honors thesis, Oberlin College

Born, M. & Wolf, E. 1999, Principles of Optics, 7th edn. (Cambridge University Press)

Brisken, W. F., Benson, J. M., Goss, W. M., & Thorsett, S. E. 2002, Astrophys. J., 571, 906

Chatterjee, S., Cordes, J. M., Lazio, T. J. W., Goss, W. M., Fomalont, E. B., & Benson, J. M. 2001, Astrophys. J., 550, 287

Clegg, A. W., Fey, A. L., & Lazio, T. J. W. 1998, Astrophys. J., 496, 253

Clegg, A. W., Fiedler, R. L., & Cordes, J. M. 1993, Astrophys. J., 409, 691

Cordes, J. M. & Lazio, T. J. W. 2002, preprint, astro-ph/0207156

—. 2003, preprint, astro-ph/0301598

Cordes, J. M. & Rickett, B. J. 1998, Astrophys. J., 507, 846

Cordes, J. M., Rickett, B. J., Stinebring, D. R., & Coles, W. A. 2004, Astrophys. J., in prep.

Cordes, J. M., Weisberg, J. M., & Boriakoff, V. 1983, Astrophys. J., 268, 370

Feynman, R. P., Leighton, R. B., & Sands, M. 1964, The Feynman Lectures on Physics, Vol. 2 (Addison-Wesley Publishing Company), ch. 7–3

Fiedler, R., Dennison, B., Johnston, K. J., Waltman, E. B., & Simon, R. S. 1994, Astrophys. J., 430, 581

Fiedler, R. L., Dennison, B., Johnston, K. J., & Hewish, A. 1987, Nature, 326, 675

Griffiths, D. J. 1999, Introduction to Electrodynamics, 3rd edn. (Upper Saddle River, New Jersey: Prentice Hall)

Higdon, J. C. 1984, Astrophys. J., 285, 109

—. 1986, Astrophys. J., 309, 342

Hill, A. S., Stinebring, D. R., Barnor, H. A., Berwick, D. E., & Webber, A. B. 2003, Astrophys. J., 599, 457

Hobbs, G., Lyne, A. G., Kramer, M., & Martin, C. E. 2003, Mon. Not. R. Astron. Soc., in prep; accessed via the ATNF Pulsar Database: `http://www.atnf.csiro.au/research/pulsar/psrcat/`

Krall, N. A. & Trivelpiece, A. W. 1973, Principles of Plasma Physics (New York: McGraw-Hill), pp. 9–12

Kramer, M. A. 2001, Honors thesis, Oberlin College

Lyne, A. G., Anderson, B., & Salter, M. J. 1982, Mon. Not. R. Astron. Soc., 201, 503

Lyne, A. G. & Graham-Smith, F. 1990, Pulsar Astronomy (Cambridge University Press)

Lyne, A. G. & Rickett, B. R. 1968, Nature, 218, 825

McKee, C. F. & Ostriker, J. P. 1977, Astrophys. J., 218, 148

Reeves, D. 2003, Honors thesis, Oberlin College

Rickett, B. J., Lyne, A. G., & Gupta, Y. 1997, Mon. Not. R. Astron. Soc., 287, 739

Stinebring, D. R., Hill, A. S., McLaughlin, M. A., Becker, K. M., & Kramer, M. A. 2004, Astrophys. J., in prep.

Stinebring, D. R., McLaughlin, M. A., Cordes, J. M., Becker, K. M., Espinoza Goodman, J. E., Kramer, M. A., Sheckard, J. L., & Smith, C. T. 2001, Astrophys. J., 549, L97

Taylor, J. H. & Cordes, J. M. 1993, Astrophys. J., 411, 674

van de Kamp, P. 1967, Principles of Astrometry (San Francisco: W. H. Freeman and Company)

Walker, M. & Wardle, M. 1998, Astrophys. J., 498, L125

Walker, M. A., Melrose, D. B., Stinebring, D. R., & Zhang, C. M. 2004, Mon. Not. R. Astron. Soc., submitted; preprint astro-ph/0403587

Weisstein, E. 2004, in Eric Weisstein's World of Physics (available at `http://scienceworld.wolfram.com/physics/PlasmaFrequency.html`)

Wolszczan, A. & Cordes, J. M. 1987, Astrophys. J., 320, L35

Index